The Astrophysical Journal, 806:109 (21pp), 2015 June 10 doi:10.1088/0004-637X/806/1/109

REST-FRAME OPTICAL SPECTRA AND BLACK HOLE MASSES OF $3 < z < 6$ QUASARS

Hyunsung David Jun[1,2], Myungshin Im[2,3,14], Hyung Mok Lee[3], Youichi Ohyama[4], Jong-Hak Woo[3], Xiaohui Fan[5], Tomotsugu Goto[6], Dohyeong Kim[2,3], Ji Hoon Kim[2,7], Minjin Kim[8,9], Myung Gyoon Lee[3], Takao Nakagawa[10], Chris Pearson[11,12,13], and Stephen Serjeant[11]

[1] Jet Propulsion Laboratory, California Institute of Technology, 4800 Oak Grove Dr., Pasadena, CA 91109, USA; hyunsung.jun@jpl.nasa.gov
[2] Center for the Exploration of the Origin of the universe (CEOU), Astronomy Program, Department of Physics and Astronomy, Seoul National University, Seoul 151-742, Korea; mim@astro.snu.ac.kr
[3] Astronomy Program, Department of Physics and Astronomy, Seoul National University, Seoul 151-742, Korea
[4] Academia Sinica, Institute of Astronomy and Astrophysics, P.O. Box 23-141, Taipei 10617, Taiwan, China
[5] Steward Observatory, The University of Arizona, Tucson, AZ 85721, USA
[6] Institute of Astronomy and Department of Physics, National Tsing Hua University, No. 101, Section 2, Kuang-Fu Road, Hsinchu, 30013, Taiwan, China
[7] Subaru Telescope, National Astronomical Observatory of Japan, 650 North A'ohoku Place, Hilo, HI 96720, USA
[8] Korea Astronomy and Space Science Institute, Daejeon 305-348, Korea
[9] University of Science and Technology, Daejeon 305-350, Korea
[10] Institute of Space and Astronautical Science, Japan Aerospace Exploration Agency, Sagamihara, Kanagawa 252-5210, Japan
[11] Department of Physical Sciences, The Open University, Milton Keynes, MK7 6AA, UK
[12] RAL Space, CCLRC Rutherford Appleton Laboratory, Chilton, Didcot, Oxfordshire OX11 0QX, UK
[13] Oxford Astrophysics, Denys Wilkinson Building, University of Oxford, Keble Rd, Oxford OX1 3RH, UK
Received 2014 December 30; accepted 2015 March 30; published 2015 June 10

ABSTRACT

We present the rest-frame optical spectral properties of 155 luminous quasars at $3.3 < z < 6.4$ taken with the *AKARI* space telescope, including the first detection of the Hα emission line as far out as $z \sim 6$. We extend the scaling relation between the rest-frame optical continuum and the line luminosity of active galactic nuclei (AGNs) to the high-luminosity, high-redshift regime that has rarely been probed before. Remarkably, we find that a single log-linear relation can be applied to the 5100 Å and Hα AGN luminosities over a wide range of luminosity ($10^{42} < L_{5100} < 10^{47}$ ergs s^{-1}) or redshift ($0 < z < 6$), suggesting that the physical mechanism governing this relation is unchanged from $z = 0$ to 6, over five decades in luminosity. Similar scaling relations are found between the optical and the UV continuum luminosities or line widths. Applying the scaling relations to the Hβ black hole (BH) mass ($M_{\rm BH}$) estimator of local AGNs, we derive the $M_{\rm BH}$ estimators based on the Hα, Mg II, and C IV lines, finding that the UV-line-based masses are overall consistent with the Balmer-line-based, but with a large intrinsic scatter of 0.40 dex for the C IV estimates. Our 43 $M_{\rm BH}$ estimates from Hα confirm the existence of BHs as massive as $\sim 10^{10}\,M_{\odot}$ out to $z \sim 5$ and provide a secure footing for previous results from Mg II-line-based studies that a rapid $M_{\rm BH}$ growth has occurred in the early universe.

Key words: galaxies: active – galaxies: evolution – quasars: emission lines – quasars: supermassive black holes

Supporting material: machine-readable table

1. INTRODUCTION

Quasars, galaxies that are in an active phase due to vigorous accretion of matter toward the central supermassive black hole (BH), have been widely discovered by many surveys (e.g., Schmidt & Green 1983; Hewett et al. 1995; Boyle et al. 2000; York et al. 2000; Richards et al. 2002; Im et al. 2007; Lee et al. 2008; Willott et al. 2010b; Wu et al. 2010). Through the discovery of quasars at high redshift (Fan et al. 2000; Cool et al. 2006; Goto 2006; Stern et al. 2007; Willott et al. 2007; Mortlock et al. 2011; Venemans et al. 2013; Bañados et al. 2014), we are witnessing the early stages of supermassive BH growth in the distant universe. The number density of optically luminous quasars at high redshift quickly increases with cosmic time toward its maximum at $z = 2 \sim 3$ (Dunlop & Peacock 1990; Warren et al. 1994; Kennefick et al. 1995; Schmidt et al. 1995; Richards et al. 2006; McGreer et al. 2013). Accompanied by high accretion rates among luminous quasars at $z > 4$ (e.g., Willott et al. 2010a; De Rosa et al. 2011, 2014), this suggests a rapid BH growth of the luminous population of active galactic nuclei (AGNs) in the early universe. Also, an unusual population of AGNs known as dust-poor quasars—quasars with little infrared emission from hot and warm dust—is found to be more common at higher redshift (Jiang et al. 2010; Jun & Im 2013; Leipski et al. 2014). Luminous dust-poor quasars tend to have lower BH masses ($M_{\rm BH}$) or higher Eddington ratios compared to typical luminous quasars (Jiang et al. 2010; Jun & Im 2013), indicating the build-up of the AGN dusty substructure during its early mass accretion.

One of the key findings in the study of high-redshift quasars is that extremely massive BHs exist with masses reaching $M_{\rm BH} \sim 10^{10}\,M_{\odot}$ at $z = 2$–5 and $\sim 10^{9}\,M_{\odot}$ at $z = 6$–7 (Jiang et al. 2007; Kurk et al. 2007; Netzer et al. 2007; Vestergaard et al. 2008; Shen et al. 2008; Mortlock et al. 2011; De Rosa et al. 2014). Under the concordance cosmology, the time gap between the reionization epoch of the universe from the recent *Planck* study of the cosmic microwave background, $z \sim 11.5$ (Planck Collaboration et al. 2014) and $z = 6$, is 0.5 Gyr. Considering the case where a Population II stellar seed $M_{\rm BH}$ starts to grow at $z \sim 11.5$, the given time is too short for the seed to become an extremely massive BH at $z = 6$. Under the Eddington-limited accretion where the mass accretes at a maximal rate with the radiative pressure gradient and gravity in

[14] Author to whom correspondence should be addressed.

balance, we expect a BH to grow as

$$M(t) = M_0 \exp\left(\frac{1-\epsilon}{\epsilon}\frac{t-t_0}{t_{\rm Edd}}\right), \quad (1)$$

where M_0 is the mass at t_0, ϵ is the radiative efficiency, and $t_{\rm Edd}$ is the Eddington-limited timescale of 0.45 Gyr. Assuming a typical value of $\epsilon = 0.1$, a BH can grow by 2×10^4 times over the time span of 0.5 Gyr, without considering feedback mechanisms that could slow down the BH growth. This maximal growth factor is far too small for a stellar mass BH with a typical seed mass of $10\,M_\odot$ to grow into the extremely massive AGNs that have been observed recently. Consequently, BH seeds that may have started accreting prior to the reionization epoch, which are more massive (e.g., Bromm & Loeb 2003; Begelman et al. 2006; Lodato & Natarajan 2006; Bellovary et al. 2011) or go through super-Eddington accretion (e.g., Volonteri & Rees 2005; Wyithe & Loeb 2012; Madau et al. 2014), are suggested to explain the $M_{\rm BH}$ of quasars at high redshift (also see a review on this subject by Natarajan 2014).

Obviously, an accurate determination of $M_{\rm BH}$ is an important requirement for understanding the BH growth at high redshift. This is especially true for BHs at the most massive end. A large uncertainty in $M_{\rm BH}$ can scatter the abundant lower-mass BHs into the high-mass end of the $M_{\rm BH}$ distribution, whereas the effect in the opposite direction is much less significant because higher-mass BHs are relatively rare. As a result, the number of extremely massive BHs can be easily overestimated. In principle, a correction to this effect is possible, but it requires a good knowledge of the error of $M_{\rm BH}$ measurements, which is, however, rather difficult to obtain. This poses a potential challenge to the understanding of BH growth at high redshift, as described below.

In most of the high-redshift quasar studies, BH masses are estimated using the rest-frame ultraviolet (UV) part of the spectra that is redshifted into the rest-frame optical (rest-optical). The velocity widths of broad UV lines such as C IV and Mg II are used as measures of the gas motion of the broad-line region (BLR), and the continuum or the line luminosity at the rest-frame UV (rest-UV) is used as a proxy for the size of the BLR ($R_{\rm BLR}$). One gets $M_{\rm BH}$ by combining the two pieces of information through a virial mass estimator: $M_{\rm BH} \propto R_{\rm BLR} \times {\rm FWHM}^2_{\rm BLR}$ (e.g., McLure & Dunlop 2004; Vestergaard 2004; Baskin & Laor 2005; Sulentic et al. 2007; Shen et al. 2008; Park et al. 2013). While UV-based $M_{\rm BH}$ estimators are useful tools to measure the $M_{\rm BH}$ of AGNs, they are secondary estimators that are derived from rest-optical spectral properties such as the line luminosity or width of Hβ and Hα and the continuum luminosity at 5100 Å (L_{5100}). Assuming that the UV luminosity follows the optical BLR radius–luminosity ($R_{\rm BLR}$–L) relation with a constant factor, and the UV broad line width follows the optical line width as a power-law relation, the UV $M_{\rm BH}$ estimators are derived. Consequently, a number of studies have been carried out to justify the use of Mg II- or C IV-line-based $M_{\rm BH}$ estimators, comparing the masses from the UV estimators to those from the optical. While some studies suggest that UV-line $M_{\rm BH}$ estimators are reasonably accurate, especially for Mg II, other studies point out a large scatter between C IV-based measurements versus Hβ-based measurements, which can make the C IV-based $M_{\rm BH}$ values uncertain by a factor of a few (e.g., Netzer et al. 2007; Shen & Liu 2012, hereafter S12). It has been noted that nonvirialized motion (e.g., Denney 2012) or extinction (e.g., Assef et al. 2011) could severely modify the C IV line profile such that the $M_{\rm BH}$ cannot be reliably measured from a simple virial equation, although the origin of the discrepancy between the UV and the optical $M_{\rm bh}$ values is unclear.

Furthermore, for the $M_{\rm BH}$ estimates to be valid, one also needs to justify the application of the low-redshift $M_{\rm BH}$ estimators to high-redshift, luminous quasars. Although one can expect that the $M_{\rm BH}$ estimators should not evolve in time in any significant way based on the physical ingredients of AGN models, this has not been tested in the high-redshift, high-luminosity regime. An ultimate test would be to perform a reverberation mapping study of high-luminosity quasars at high redshift, but such a study would take decades to complete because the variability timescale is long for luminous quasars, and the cosmological time dilation makes it even longer. Another way, albeit less direct than the reverberation mapping method, would be to investigate the correlation between the line and continuum luminosities. At low redshift, the Hα or Hβ line luminosities are known to tightly correlate with the optical continuum luminosity (e.g., Greene & Ho 2005). As the radiation energy L from an accretion disk increases, the distance to the BLR increases as $R \propto L^{0.5}$ from a simple photoionization argument, or the energy flux of the radiation incident upon BLR clouds would be independent of the luminosity of the central power source, which has been confirmed observationally (Kaspi et al. 2000, 2005; Bentz et al. 2013). A modification in the $R_{\rm BLR}$–L relation at high redshift or high luminosity, for example, would result in an increase or a decrease in the energy flux incident upon the BLR, and thus the correlation between the line and continuum luminosities is likely to be modified. Interestingly, several studies suggest that the $R_{\rm BLR}$–L relation is not valid for luminous AGNs having massive BHs with low spins (Laor & Davis 2011; Wang et al. 2014), due to a decrease in the ionizing flux $L_{\rm ion}$ caused by a decrease in the radiation temperature of the accretion disk. Because the line luminosity $L_{\rm line}$ is proportional to $L_{\rm ion}$, such theoretical expectations can be tested by examining the $L_{\rm line}$–L_{5100} relation at the luminous end.

In order to estimate the $M_{\rm BH}$ using an optical mass estimator and to test the universality of the scaling relations in the rest-optical for quasars at $z > 3.5$, a spectroscopic observation is necessary at $\lambda > 2.5\,\mu$m. This however, is a very challenging task from the ground because of the high thermal background at $\lambda > 2.5\,\mu$m and atmospheric absorptions, limiting such efforts to the study of the Hβ line at $z < 3.5$ (e.g., Shemmer et al. 2004; Netzer et al. 2007; Assef et al. 2011). Recently, *AKARI* spectroscopic observations have provided a breakthrough for the study of the rest-optical spectra of distant objects, where its unique 2.5–5.0 μm coverage enables the redshifted Hα line to be probed from $z = 3$ to 6.5. Oyabu et al. (2007) reported the *AKARI* detection of the redshifted Hα line of the quasar RX J1759.4+6638 at $z = 4.3$, and Sedgwick et al. (2013) investigated the star-formation rate of submillimeter -galaxies at $z > 3.5$ based on Hα.

With one of the *AKARI* mission programs (guaranteed time) and also through several small open time programs, we performed a spectroscopic study of quasars at high and low

redshifts, with the aim of obtaining the rest-optical spectra of high-redshift quasars or the rest-frame 2.5–5.0 μm spectra of low-redshift AGNs. We call all of these programs Quasar Spectroscopic Observations with NIR Grism (QSONG) after the name of the mission program, and here we present the rest-optical spectral properties of 155 type-1 quasars from QSONG, along with scaling relations and $M_{\rm BH}$ estimates based on these spectra.

The contents of this paper are organized as follows. First, we use the spectrophotometric data including *AKARI* for $z \gtrsim 3$ AGNs (Section 2), and we derive the continuum and line emission properties (Section 3) in order to calibrate the Hα $M_{\rm BH}$ for use at high redshift. We check the validity of the continuum and broad line luminosity relations and line width relations with respect to the local, update the mass equations for Hα, Hβ, Mg II, and C IV, and compare the UV–optical $M_{\rm BH}$s (Section 4). Finally, we discuss the reliability of single-epoch $M_{\rm BH}$ estimators at high redshift and investigate the massive end evolution of $M_{\rm BH}$ in distant AGNs (Section 5). Throughout this paper, we adopt a flat ΛCDM cosmology with parameters of $H_0 = 70$ km s^{-1} Mpc^{-1}, $\Omega_m = 0.3$, and $\Omega_\Lambda = 0.7$. For the virial factor in the $M_{\rm BH}$ estimator, we adopt $f = 5.1 \pm 1.3$ based on the calibration of the $M_{\rm BH}$–σ relation using the combined sample of AGNs and quiescent galaxies by Woo et al. (2013).

2. DATA

2.1. Sample

The majority of the data comes from the *AKARI* program QSONG, which is a two-year, warm (phase-3) mission program consisting of ∼900 approved pointings, or ∼150 hours of observations. The program is aimed at obtaining the rest-optical spectra of high-redshift AGNs (Jun et al. 2012) or the 2.5–5.0 μm spectra of low-redshift AGNs (Kim et al. 2015) containing Brackett and 3.3 μm polycyclic aromatic hydrocarbon lines. The sample for this study is limited to the high redshift, occupying 65% of the entire QSONG data. It is composed of optically luminous and spectroscopically confirmed type-1 quasars at $z \gtrsim 3$, mostly out of the Sloan Digital Sky Survey (SDSS) (DR5 catalog, Schneider et al. 2007; and additional discoveries from Fan et al. 2000, 2001, 2003, 2004, 2006) and Automated Plate Measuring UK Schmidt Telescope (APM-UKST; Storrie-Lombardi et al. 1996, 2001) surveys. Additional targets are from various references (Webb et al. 1988; Gregory & Condon 1991; Henry et al. 1994; Griffith et al. 1995; Kennefick et al. 1995; Djorgovski et al. 1998; Rengstorf et al. 2004; McGreer et al. 2006).

The targets are type-1 AGNs, so they allow the $M_{\rm BH}$ estimation from the broad line kinematics, through Hα/Hβ appearing within the *AKARI* near-infrared (NIR) spectral coverage. In order to provide a minimal sensitivity limit to the sample, we first considered the aperture size (68 cm) of the telescope and the restricted exposure time available at each sky position. After simulating the rest-optical spectra under the expected *AKARI* signal-to-noise ratio (S/N), the targets were chosen with z-band flux limits of ∼18.5 and 19 AB magnitudes for bright and faint subsamples, respectively, with the longer exposure time assigned to fainter targets for a clear line detection. Moreover, the targets were bounded in $3.3 < z < 6.4$ so that the Hα emission and the surrounding continuum are placed within the 2.5–5.0 μm window of *AKARI* NIR spectroscopy. Without further constraints, the targets were randomly selected in coordinates, redshift, and luminosity. We plot the distribution of z–$L_{5100\ \text{Å}}$ in Figure 1.

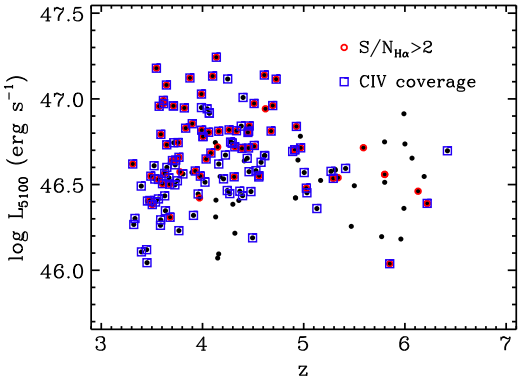

Figure 1. 5100 Å luminosity–redshift distribution of our *AKARI* observed quasars (black dots). The subsamples with $S/N_{H\alpha} > 2$ are pointed in red, and objects with rest-UV spectral coverage including the C IV emission are marked as blue squares.

Following the Hα observations of distant AGNs from *AKARI* NIR spectroscopy (Oyabu et al. 2007; Oyabu et al. 2009), our initial Hα survey of 14 quasars at $z \sim 6$ under the helium-cooled (phase-2) open time program HZQSO (Im 2010), demonstrated the feasibility of *AKARI* observations in detecting the redshifted Hα emission. QSONG is essentially a phase-3 extension of the survey, for the purpose of vastly expanding the number of targets at the expense of warm phase sensitivity. Thus it probes a lower redshift distribution of quasars than does HZQSO, with a peak at $z \sim 4$. In addition, two more phase-3 open time programs, HQSO2 and DPQSO, were carried out either to push the redshift limit of QSONG or to detect fainter optical lines (Hβ and [O III]) from deep exposures. Unfortunately, the helium-dry observations led to significantly higher noise levels than expected, restricting the distinct scientific goals of the phase-3 programs that required better sensitivity. Therefore, we decided to merge all open time programs listed above under the scope of QSONG.

2.2. Data Acquisition

We mostly used the NIR grism (NG) mode of the Infrared Camera (IRC, Ohyama et al. 2007; Onaka et al. 2007) on board the *AKARI* satellite (Murakami et al. 2007). It offers a low, wavelength-dependent spectral resolution (R), where $R = 120$ at 3.6 μm. This corresponds to a velocity resolution of 2500 km s^{-1} in FWHM, sampled by a pixel scale of 0.0097 μm in wavelength. The targets were placed in a $1' \times 1'$ rectangular slit aperture to reduce source confusion. The wavelength dependence of R can be expressed as $R = 120$ (λ/3.6 μm) because the dispersion is nearly a constant (Sakon et al. 2012). Meanwhile, a limited number of NIR prism (NP, $R = 19$ at 3.5 μm) observations were performed to better catch the fainter continuum and line luminosities. The angular pixel scale is 1.″5 such that all targets are point-like in our probed redshifts.

The observations were performed under the Astronomical Observation Template (AOT) mode of AOT04, typical for spectroscopic observations. The number of NG pointings per target was normally three to five for QSONG, where one pointing observation corresponds to a 355 or 400 s on-source exposure. The number of pointings were determined based on the z-band flux, generally set to be smaller for phase-2 and

Table 1
Summary of Observations

Program Name	Phase	Observed Period	Mode	Number of Targets	Observed Pointings	Rejected Pointings
HZQSO	2	2006 Nov–2007 Aug	NG	7	26	2
			NP	5	16	7
QSONG, HQSO2, DPQSO	3	2008 Jun–2010 Jan	NG	147	622	74
			NP	6	11	3

Note. NG and NP stand for NIR grism and prism modes, while a pointing is about 10 minutes long. For the QSONG program data, only the high-redshift subsample is noted. The total number of targets is 165, excluding 22 rejected sources from confusion, problems in the spectra, or data reduction (Section 2.3). Ten objects are either duplicated or different in the observing mode or program, yielding an effective total of 155 independent objects.

larger for phase-3 open time programs. The NP observations were performed with usually one or two pointings. By the time of termination of the satellite mission, the QSONG program was 85% complete with 144 high-redshift quasars observed. The open time programs were complete before the satellite lifetime, adding another 33 targets. Table 1 summarizes the observations.

To supplement the NIR spectra, we compiled the optical spectra of the *AKARI* quasars from the SDSS database (DR10 including both the SDSS-I/SDSS-II and the SDSS-III BOSS data; Ahn et al. 2014) and from observations of APM-UKST quasars (Storrie-Lombardi et al. 1996; Péroux et al. 2001) and Q0000–26 (Schneider et al. 1989), in order to estimate the C-line-based $M_{\rm BH}$. Also, we collected broadband photometric data from optical to mid-infrared (MIR) imaging, for the calculation of the rest-frame UV–optical continuum luminosity of AGNs through spectral energy distribution (SED) fitting (Section 3.2). The data includes the SDSS DR9, 2MASS PSC, UKIDSS DR10, and *WISE* AllWISE releases (Skrutskie et al. 2006; Lawrence et al. 2007; Wright et al. 2010; Ahn et al. 2012) and existing Pan-STARRS, *Spitzer*, and *AKARI* imaging (Hines et al. 2006; Jiang et al. 2006; Oyabu et al. 2009; Jiang et al. 2010; Leipski et al. 2014). The Galactic extinction is corrected for these spectrophotometric data, assuming the total-to-selective extinction ratio of $R_V = 3.1$ and using the corrected form (Bonifacio et al. 2000) of the extinction map values of Schlegel et al. (1998). The photometric measurement schemes are different in each survey, such that host galaxy contamination may not be well subtracted. We keep the diverse magnitude type and imaging resolution of each of the survey data, however, as the high-luminosity AGNs yield a compatible set of magnitudes dominated by the central AGN contribution (Jun & Im 2013). The optical spectra and the multiwavelength imaging data are outlined in Table 2.

Table 2
Supplementary Data

Name	Wavelength	*N*	Exposure	Reference
Spectra				
SDSS	3800–9200 Å	111	⩾45 m	1
BOSS	3650–10400 Å	98	⩾45 m	1
APM-UKST	~3500–9000 Å	16	15–60 m	2, 3
Hale	4500–9000 Å	1	30 m	4
Photometry				
SDSS	*ugriz*	134	54 s	5
Pan-STARRS	*zy*	14	6 m	6
2MASS	*JHK*	76	8 s	7
UKIDSS	*YJHK*	34	40 s	8
WISE	*W*1–*W*4	161	200 s	9
Spitzer	IRAC, MIPS 24 μm	27	17–23 m	6, 10, 11, 12
AKARI	IRC 2–11 μm	1	⋯	13

Note. *N* is the number of matches to the 165 *AKARI* objects in Table 1. Exposure times are typical values.
References. (1) Ahn et al. (2014), (2) Storrie-Lombardi et al. (1996), (3) Péroux et al. (2001), (4) Schneider et al. (1989), (5) Ahn et al. (2012), (6) Leipski et al. (2014), (7) Skrutskie et al. (2006), (8) Lawrence et al. (2007), (9) Wright et al. (2010), (10) Hines et al. (2006), (11) Jiang et al. (2006), (12) Jiang et al. (2010), (13) Oyabu et al. (2007).

2.3. Data Reduction

The data were reduced using the automated IDL pipeline package IRC_SPECRED (versions 20110114, 20111121 for phase 2 and 3; Ohyama et al. 2007), where preprocessing (dark, linearity, flat corrections), image registration and coaddition, flux and wavelength calibration, astrometry, spectral extraction, and aperture correction were the main tasks involved. The standard pipeline configuration was adopted, except for the use of a short exposure when the images taken for registering subframes of spectral data were contaminated by saturated stars. This procedure considerably improved the registration of two-dimensional (2D) spectra in both the spatial and wavelength directions. In addition, astrometry of the reference image was upgraded using the Two Micron All Sky Survey (2MASS) point source catalog to better extract the faint NIR spectra. Indeed, the zeroth-order positions of the spectra and the 2MASS coordinates were visually well aligned for spectral extraction.

Because of the increased number of hot pixels and the background level in the phase-3 data, a nonnegligible number of bad pixels remained in the reduced spectral data, even after applying the IRC_SPECRED pipeline. To remove the remaining hot pixels, a further data-reduction step was taken to obtain a cleaner set of spectra, as depicted in Figure 2. After running the spectroscopic pipeline, we subtracted the remaining hot pixels using L.A.Cosmic (van Dokkum 2001) with a threshold of 2.5σ and combined the one-dimensional (1D) spectra with a 2.5σ clipping. This threshold was chosen by visually inspecting the reduced spectra so that the chosen threshold removes the spiky hot pixels efficiently without affecting the emission lines. Because the typical FWHM of the broad lines in our AGNs is broader than the spectral resolution of NG ($2500\,{\rm km\,s^{-1}}$) but not that of NP ($15{,}800\,{\rm km\,s^{-1}}$ at $3.5\,\mu$m), the hot pixel rejection and the sigma clipping were applied to the NG data only, while the undersampled NP emission spectra were kept unchanged. We clipped 2.7% and 2.9% of the NG spectral data through the hot pixel reduction procedure and the combining process, respectively.

We extracted the 1D spectra of three-pixel width for the phase-2 data to maximize S/N, but the width was widened to five pixels for the phase-3 data because the noisier spectra

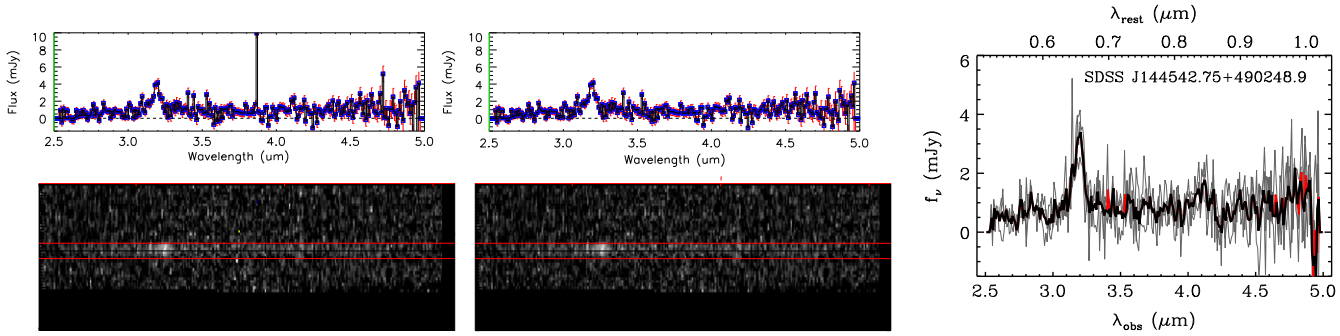

Figure 2. Sequential visualization of the data treatment additional to the pipeline processing. From the pipeline processed spectrum (left, 1D at top and 2D at bottom), hot pixels were rejected (center) before the spectral extraction within the aperture mask (red lines). The multiple pointings extracted (right, gray lines) were stacked (thick black line) with the sigma clipping (red line indicates clipped data).

made it difficult to determine the center of the object spectrum. Host galaxy contamination is negligible at the bright luminosities of the sample quasars (S11), enabling flexible extraction widths. Aperture corrections were automatically carried out from the pipeline to derive the total flux, for given respective extraction widths. The pipeline did a fair job of placing the extraction aperture on the right location, but visual inspection showed it necessary to make a −1 pixel shift in the spatial direction for 90% of the sample. For 10% of the cases, a different shift of −2–1 pixels was necessary. The wavelength zero points were determined from the pipeline, taking into account the satellite attitude drift and subpixel coordinate rounding effects, and we did not apply any further correction because the zero points were confined within a 0.5 pixel scatter.

Multiple pointings of the 1D spectra were stacked for each object, where the NG spectra were interpolated to a fixed wavelength grid, flux averaged, and error rescaled assuming Poisson error statistics. Multiple pointings of NP spectra were stacked without modifying the individual spectrum because of their poor resolution. We provided secondary flux calibration to the stacked spectra by integrating the *AKARI* fluxes over the *WISE* filter response curves, to match the *W1* and *W2* fluxes together by a constant additive correction. The average and rms scatter of the corrections are -0.01 ± 0.19 mJy. Out of 675 pointing observations, we used 589 pointings from 165 objects, since some of the pointing observations were not usable because of contamination of the object spectrum by adjacent sources. We excluded frames from the analysis when there was a source that is brighter than the target and its distance from the target is less than the FWHM in the spatial direction. On rare occasions, the reduction pipeline did not run properly, and such data were not used. In Figure 3, we plot the histogram of $S/N_{H\alpha}$, the S/N of the Hα emission line measured within $\pm$ $FWHM_{H\alpha}$ from the line center.

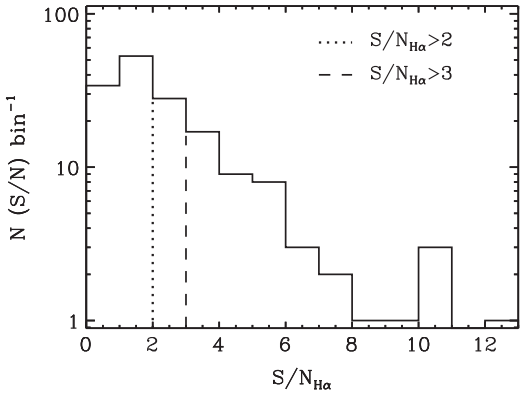

Figure 3. $S/N_{H\alpha}$ distribution of the 160 *AKARI* observed quasars with available S/N (Section 3.1). The $S/N_{H\alpha} > 2$ and >3 cuts are marked with dotted and dashed lines, which are given to limit the measurement of $L_{H\alpha}$ and $FWHM_{H\alpha}$, respectively (Figure 5).

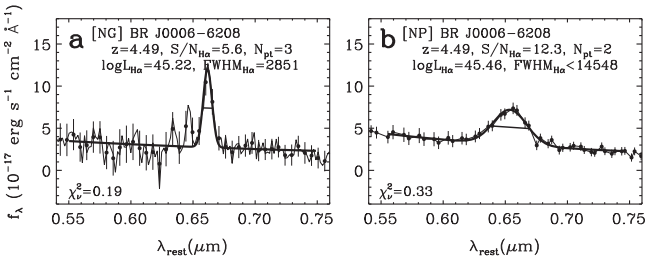

Figure 4. Examples of the rest-frame Hα emission fitting. On top of the spectra (thin line), the resolution (three-pixel) matched data (dots) and errors, the best fit to the continuum and Hα line emission (thick line), and FWHM are indicated. On the figures, the observation mode, the name of the object, the redshift and S/N of the Hα emission, the number of *AKARI* pointings, N_{pt}, Hα luminosity (ergs s^{-1}), and FWHM (km s^{-1}) are printed. The (a) NG and (b) NP observations performed for BR J0006–6208 gives an idea of the enhanced resolution and sensitivity of each spectroscopic mode.

3. ANALYSIS

3.1. Spectral Fitting

We modeled the rest-frame 5500–7500 Å spectra of our AGNs as a sum of the power-law continuum $f_\lambda = c\,\lambda^{-(2+\alpha)}$ (where $f_\nu \propto \nu^\alpha$) and the Gaussian Hα emission components. We did not attempt to fit the relatively weak emission features far (He I, [O I]) or near the Hα ([N II] and [S II] doublets, Fe II complex) because they were not detectable under the *AKARI* spectroscopic resolution and sensitivity. Likewise, the Hβ and [O III] lines were too weak to be detected in most cases and were not fitted accordingly. Examples of the fitting are given in Figure 4, with fitted parameters shown on each panel. We found that 23% of the sample show spiky emission/absorption features around the Hα line from low S/N spectra, which were manually masked out. The Hα line was modeled as a single broad Gaussian with observed FWHMs of 2500–10,000 km s^{-1} for the inability to clearly resolve the narrow or multiple broad components at $R \sim 120$. The Hα line center was set free within $\pm$2500 km s^{-1} to the UV-line-based redshift from the references in Table 2. However, we found four (SDSS J143835.95+431459.2, SDSS J142243.02

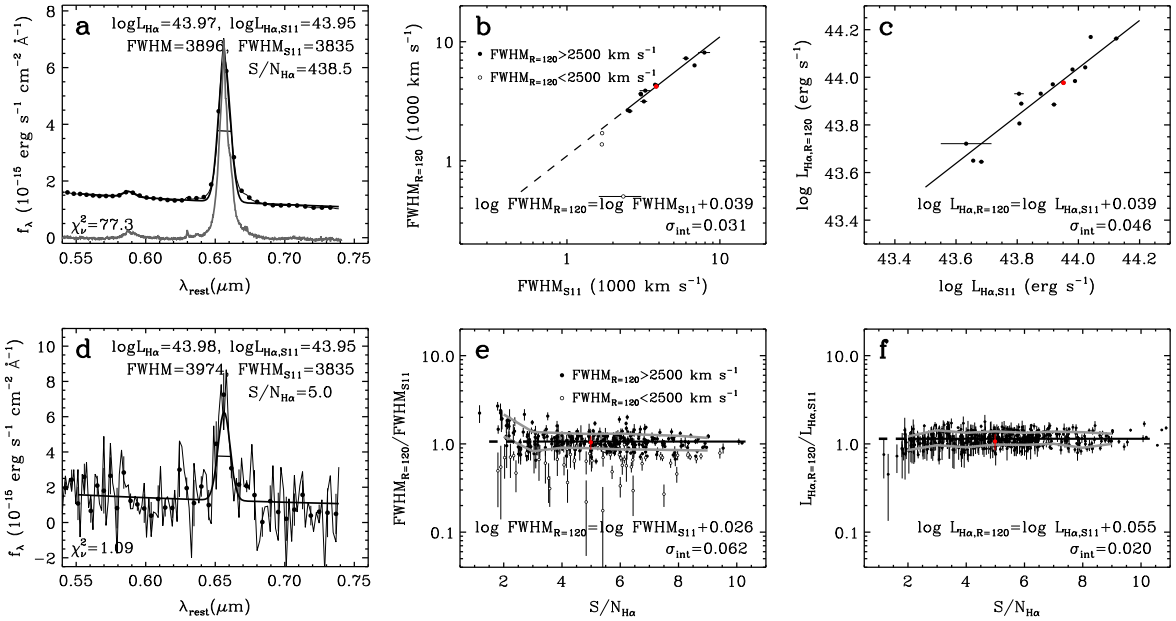

Figure 5. Top row: an example fit to the resolution-degraded SDSS spectrum to test the reliability of M_{BH} from *AKARI* observations (left), where the continuum-subtracted original SDSS spectrum (gray) and the *AKARI* resolution-matched spectrum (black dots) with fit to the simulated data (thick line) are plotted. The broad FWHM$_{H\alpha}$ values of $z < 0.3$, $L_{5100} > 10^{45}$ ergs s^{-1} SDSS quasars from S11 are compared to our fitting result of the simulated spectrum (center). Offsets from a one-to-one relation and intrinsic scatter are displayed. For the comparison of FWHMs (center), we divide the sample into FWHM$_{H\alpha}$ larger or smaller than 2500 km s^{-1} (filled and open dots) and only use the FWHM$_{H\alpha}$ > 2500 km s^{-1} data. The red highlighted symbol represents the example on the left-most panel. Likewise, the Hα luminosity from S11 and our single Gaussian fit to the simulated spectra are compared (right). Bottom row: we also test the effect of low S/N on the fitting by adding a set of Gaussian random noise to the resolution-degraded spectrum (left). The ratio of our FWHM$_{H\alpha}$, $L_{H\alpha}$ measurements to that from S11 are plotted along the S/N$_{H\alpha}$ (center and right). For the comparison of FWHMs (center), we remove 49 data points from the plot with ΔFWHM$_{H\alpha} = 0$ usually at FWHM$_{H\alpha}$ < 2500 km s^{-1}. The mean and 1σ offsets are shown as black and gray lines. When calculating the mean and intrinsic scatter of the quantities, only the S/N$_{H\alpha}$ > 3, FWHM$_{H\alpha}$ > 2500 km s^{-1} data are used for the comparison of FWHM$_{H\alpha}$ and the S/N$_{H\alpha}$ > 2 and any FWHM$_{H\alpha}$ data for the $L_{H\alpha}$.

+441721.4, BR J0307–4945, and SDSS J150654.54 +522004.6) exceptions whose Hα line centers were significantly redshifted from the UV-line-based redshifts. In these cases, the velocity range was loosened to $\pm$10,000 km s^{-1}, where the Hα showed velocity shifts of 3600–5600 km s^{-1}. Next, the measured broad line width FWHM$_{obs}$ was subtracted by the instrumental resolution FWHM$_{ins}$ (Section 2.2) in quadrature, to obtain the intrinsic line width FWHM = $\sqrt{(\mathrm{FWHM_{obs}})^2 - (\mathrm{FWHM_{ins}})^2}$.

Extracting the broad emission line luminosity and width is important in accurately estimating the M_{BH} of AGNs. The limited *AKARI* sensitivity (Figure 3) and spectral resolution could produce a systematic bias in the measurement of line parameters, such as the line luminosity and width (e.g., Denney et al. 2009). Therefore, we investigated how the low-resolution, low-S/N spectra systematically affect the results of the spectral fitting. This was done by running Monte Carlo simulations on a set of luminous SDSS quasar spectra (DR7, Schneider et al. 2010) of $R \sim 2000$ to mimic the quality of *AKARI* spectra. Given that the host galaxy contamination to the quasar spectrum is negligible at $L_{5100} > 10^{45}$ ergs s^{-1} (Shen et al. 2011, hereafter S11), we collected 15, $L_{5100} > 10^{45}$ ergs s^{-1}, type-1 quasar spectra with a continuum sensitivity of S/N > 20, where the Hα emission region is present ($z < 0.3$) and well fit ($\chi^2_\nu < 2$) from S11.

We smoothed the SDSS spectra with a Gaussian function to match the *AKARI* NG resolution, $R = 120$, and rebinned the data to match the three pixels per resolution sampling of the *AKARI* spectra. First, we looked into the question of how the results are affected with a single Gaussian fit to the emission line in the low resolution of the AKARI data. For this, without adding extra noise, we followed the same method to measure the Hα line FWHM and luminosity as for the *AKARI* spectra (e.g., Figure 5(a)). In Figures 5(b) and (c) we compare the fitted parameters FWHM$_{H\alpha}$ and $L_{H\alpha}$ from the smoothed and binned spectra to that of the measurement from S11. We find that the FWHM at >2500 km s^{-1} and the line luminosity from the degraded resolution spectra are remarkably consistent with S11 within ~0.04 dex offset and intrinsic scatter σ_{int}, where $\sigma^2_{int} = \Sigma_{i=1}^{N}[\{y_i - f(x_i)\}^2 - \Delta y_i^2 - \beta^2 \Delta x_i^2]/(N-1)$ for $f(x) = \alpha + \beta x$ and a set of N data points (x_i, y_i) with measurement errors $(\Delta x_i, \Delta y_i)$. This could bias the M_{BH} measurements up to ~0.1 dex in offset and σ_{int} when following the $M_{BH} \sim L^{0.5} \times \mathrm{FWHM}^2$ behavior, but this is smaller than the typical M_{BH} measurement uncertainty (e.g., Figure 14(c)). Exceptions to the consistency between the simulated and observed parameters are the line width measurements at FWHM$_{H\alpha}$ < 2500 km s^{-1}, where the simulated FWHM values fall below the extrapolated linear relation. Therefore, we give a FWHM$_{H\alpha}$ > 2500 km s^{-1} limit to our *AKARI* data to restrict the sample with less biased line width measurements. Meanwhile, the narrow Hα and [N II] doublet luminosities of the fiducial SDSS AGNs add up to the broad $L_{H\alpha}$ by less than 0.01 dex altogether. The weakness of the narrow emission lines in luminous AGNs guarantees that the narrow line contaminations to the degraded resolution spectra are negligible.

Second, to investigate the effect of low S/N on the fitted results, we added a set of random Gaussian noises on top of the degraded resolution spectra. Each SDSS spectrum was repeatedly simulated 30 times, adding the random errors, for the S /N$_{H\alpha}$ to be distributed down to the level of *AKARI* S/N. Again, we followed the same method to measure the Hα line

FWHM (only for the $\mathrm{FWHM}_{\mathrm{H}\alpha} > 2500\,\mathrm{km\,s^{-1}}$ objects from Figure 5(b)) and luminosity as for the *AKARI* spectra (e.g., Figure 5(d)). In Figures 5(e) and (f) we plot the ratios of $\mathrm{FWHM}_{\mathrm{H}\alpha}$ and $L_{\mathrm{H}\alpha}$ from the degraded resolution and S/N spectra, to that from S11, along $\mathrm{S/N}_{\mathrm{H}\alpha}$. Overall, we find both $\mathrm{FWHM}_{\mathrm{H}\alpha}$ and $L_{\mathrm{H}\alpha}$ to be within 0.02 dex in the mean offset to the values before adding the noises (Figures 5(b) and (c)) at $\mathrm{FWHM}_{\mathrm{H}\alpha} > 2500\,\mathrm{km\,s^{-1}}$, $\mathrm{S/N}_{\mathrm{H}\alpha} > 3$ for the $\mathrm{FWHM}_{\mathrm{H}\alpha}$ and $\mathrm{S/N}_{\mathrm{H}\alpha} > 2$ for the $L_{\mathrm{H}\alpha}$. Also, the σ_{int} in $\mathrm{FWHM}_{\mathrm{H}\alpha}$ and $L_{\mathrm{H}\alpha}$ under low S/N are within 0.03 dex of those of the noise-free, effectively not changing the bias in the M_{BH} at a similar ~0.1 dex. We note that below the S/N or FWHM limit the fitted quantities systematically diverge from those calculated with the original spectrum. Therefore, we conclude that for a given selection of data neither the poor resolution nor sensitivity biases the fitted results by greater than a ~0.1 dex level of systematic offset or scatter in M_{BH}, and we give the corresponding FWHM and S/N cuts to the *AKARI* data.

Having tested the reliability of fitted quantities under possible systematic biases, we come back to the fitting of the *AKARI* data and find the fit to converge for 160 out of 165 objects. Five failures show noisy spectra near the Hα and were removed. The goodness of the spectral fitting is quantified as the reduced chi-square, and it reaches down to $\chi^2_\nu = 0.33$ in median. The fraction of AGNs passing the reliability limit for the FWHM measurements ($\mathrm{S/N}_{\mathrm{H}\alpha} > 3$) are 67% ($N = 8$) and 25% ($N = 37$) for the phase-2 and phase-3 data, respectively. Also, we flagged the five NG objects of $\mathrm{FWHM}_{\mathrm{int}} < 2500\,\mathrm{km\,s^{-1}}$ with an upper limit of $2500\,\mathrm{km\,s^{-1}}$ and put upper limits on the measured FWHM of the four NP sources (e.g., Figure 4(b)). In total, there are 43 $\mathrm{FWHM}_{\mathrm{H}\alpha}$ measurements, including seven out of nine upper limits, where the excluded two upper limits are NP measurements with overlapping coverage in NG.

Next, we computed the Hα line luminosity $L_{\mathrm{H}\alpha}$ and the 5100 Å continuum luminosity L_{5100} from the spectra, converting the measured rest-frame fluxes using the luminosity distance and assuming isotropic radiation. The $L_{\mathrm{H}\alpha}$ was derived from the Gaussian fit to the observed flux. The reliability limit for $L_{\mathrm{H}\alpha}$ ($\mathrm{S/N}_{\mathrm{H}\alpha} > 2$) is satisfied for 45% ($N = 72$) of the data, whereas the $\mathrm{S/N}_{\mathrm{H}\alpha} < 2$ spectra were provided with 2σ upper limits from their given noise levels collected within $\pm 4000\,\mathrm{km\,s^{-1}}$ of the Hα line center. Meanwhile, the L_{5100} was calculated from the average of the rest-frame fluxes at 5000–5200 Å to reduce the measurement uncertainty. The L_{5100} measurements were kept only when $\mathrm{S/N}_{5100} > 2$, and the rest of the data were given with 2σ upper limits like $L_{\mathrm{H}\alpha}$. We have fewer L_{5100} measurements than $L_{\mathrm{H}\alpha}$ where only 25% ($N = 41$) meet $\mathrm{S/N}_{5100} > 2$, not to mention the limited number of spectra (53%, $N = 88$) covering the rest-frame 5100 Å. Thus, we also derived the L_{5100} alternatively by the photometric SED fitting (Section 3.2).

In addition, we fitted the C IV region (rest-frame 1445–1705 Å) of 121 objects with an SED model containing a power-law component and double broad Gaussians to model the C IV emission. Also, a single broad Gaussian was used to fit the 1600 Å feature (Laor et al. 1994) and the He II and O III] around 1650 Å altogether because these emissions are blended but relatively detached from the C IV. This component was not regarded as a part of the C IV, consistent with the previous studies (e.g, prescription A of Assef et al. 2011; S12). We do not subtract the broad Fe II complex around the C IV emission because it does not change the $\mathrm{FWHM}_{\mathrm{C\,IV}}$ meaningfully (S11). The optical spectra were fitted after carefully masking out the absorption features around the C IV line for 25% of the spectra. Meanwhile, 16 spectra without error information were fitted assuming the flux error is uniform at all wavelengths, and the rms scatter of the best-fit solution is chosen to be the flux error afterward. Out of five spectra with severe broad absorption line (BAL) features, we fitted the C III] λ1908 and used its line width as an effective $\mathrm{FWHM}_{\mathrm{C\,IV}}$ surrogate (S12) for two objects, while excluding the remaining three objects from the UV line analysis. In total, we derived $\mathrm{FWHM}_{\mathrm{C\,IV}}$ and L_{1350} for 118 objects. The L_{1350} and its error were calculated from the average of the rest-frame 1350 ± 15 Å fluxes to avoid contamination from narrow absorption, while for seven BAL quasars we extrapolated the continuum around the C IV emission to 1350 Å. When spectra of an object were available from both SDSS-I/SDSS-II and BOSS, we performed the fit to the spectra from each data set separately and took the average of the parameter values from the independent fits. We plot examples of the spectral fitting of the Hα region in Figure 6, and of the C IV in Figure 7.

3.2. Broadband SED Fitting

The photometry data sets in Table 2 cover a wide wavelength range in broadband filters from the *u* band through 24 μm, so we fitted the broadband SEDs to provide further information on the AGN continuum luminosities. Under a photometric sensitivity limit of S/N > 5 for the observed optical–NIR and S/N > 2 in the MIR, and further rejecting the 2MASS data with a single filter detection, we modeled the SED in the rest-frame 0.3–5 μm, including five data points on average, as a sum of a power-law continuum and a blackbody emission from hot dust of $T = 1250$ K (e.g., Jun & Im 2013). For 53% of the cases ($N = 87$) for which there were no rest-frame 0.3–0.6 μm data points available, we used the average continuum slope $\alpha = -0.08$ of luminous SDSS quasars (Jun & Im 2013). The uncertainty in fixing the continuum slope was tested from objects that cover the rest-frame 0.3–0.6 μm and comparing the L_{5100} with and without fixing the α value. The test yields the L_{5100} to be offset by -0.01 ± 0.04 dex when α is fixed, compared to when α is free. Because the offsets are small, we find our method to fix the α when missing the photometric coverage near the rest-5100 Å to be reliable in tracing the L_{5100}. In addition, considering the filter bandwidths and the AGN line equivalent widths from Vanden Berk et al. (2001), we find the Hα to be the only line that meaningfully contributes to the rest-optical photometry over the continuum emission (by >0.03 dex). Thus, we removed the data point enclosing the Hα emission when the χ^2_ν containing that data point became larger than that without. Through this procedure we obtained 164 photometrically derived L_{5100}, while removing one object without any detections in the rest-frame 0.3–5 μm under our sensitivity limit. Examples of the broadband SED fitting are shown in Figure 8. The reduced chi-square values have a median of $\chi^2_\nu = 3.6$, which is acceptable given the simplification of the SED model that does not take into account the emission line features and the general agreement of the fit to the data demonstrated in Figure 8.

Meanwhile, we interpolated the broadband SED around the rest-frame 1350 and 3000 Å to obtain L_{1350} and L_{3000}. For this, we used objects with more than two data points in the rest-frame 500–2500 Å for L_{1350} or 2000–6000 Å for L_{3000}. The

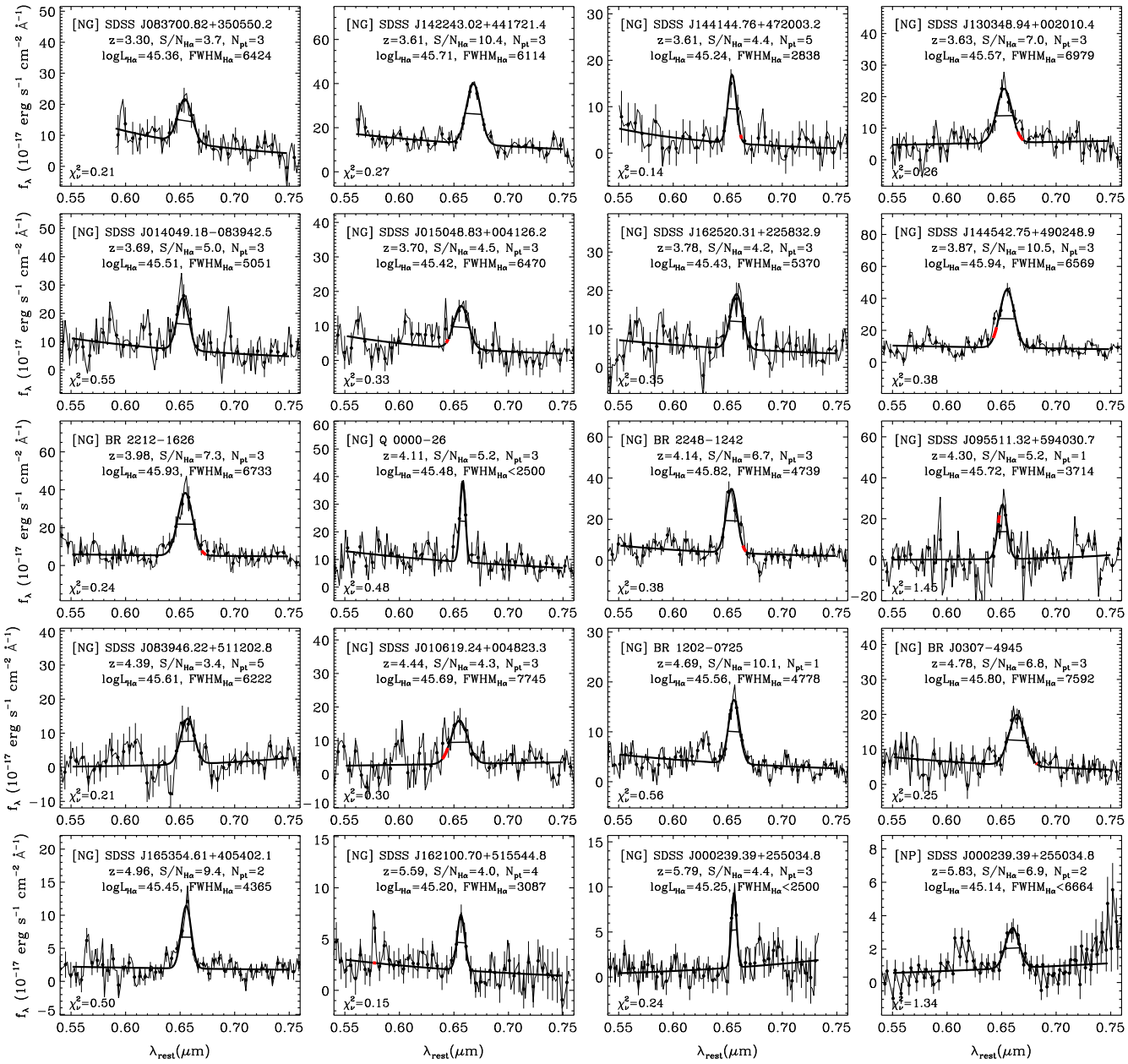

Figure 6. Rest-frame Hα spectral fitting of selected objects with S/N$_{H\alpha} > 3$, sorted by the Hα redshift. The data point symbols and colors follow the meaning of Figure 4. When there were contaminations to the Hα emission, we masked out the region (red).

interpolation is done linearly to the data points, and we obtain 137 L_{1350} and 47 L_{3000} values. The continuum luminosities derived by photometric and spectroscopic methods roughly agree with each other, as shown in Figure 9 for L_{1350} and L_{5100}, though there are not enough data points ($N = 2$) to plot for L_{3000}. Likewise to L_{5100}, we calculated the level of C IV or Mg II line contamination to the L_{1350} and L_{3000} from broadband photometry. The C IV and Mg II elevate the observed broadband flux by up to 0.06 and 0.04 dex. Thus, it is possible that the photometry embracing the broad UV emission is boosted by more than the typical measurement error in L_{1350} and L_{3000}, which are 0.02 and 0.03 dex, respectively. Between the spectroscopically and photometrically derived continuum luminosities, we will use in the following discussion the spectroscopically derived L_{1350} and the photometrically derived L_{3000} and L_{5100}. We do so because the line contaminations near 1350 Å through the broadband photometry can be significantly larger than the measurement uncertainty, whereas this is not so around the Mg II and Hα lines. The large error in L_{5100} from the *AKARI* spectra is also another reason that we opt to use L_{5100} from the broadband SED fitting. The fitted properties from this section and the M_{BH} to appear in Section 4 are listed in Table 3. For objects with both NG and NP observations, we use the $z_{H\alpha}$ and FWHM$_{H\alpha}$ from the NG and the $L_{H\alpha}$ from the NP when S /N$_{H\alpha} > 3$, and we list only the values from the NG otherwise.

4. RESULTS

4.1. Composite Spectra

To investigate the overall rest-optical spectral properties of the sample, we construct the composite *AKARI* spectra. Out of

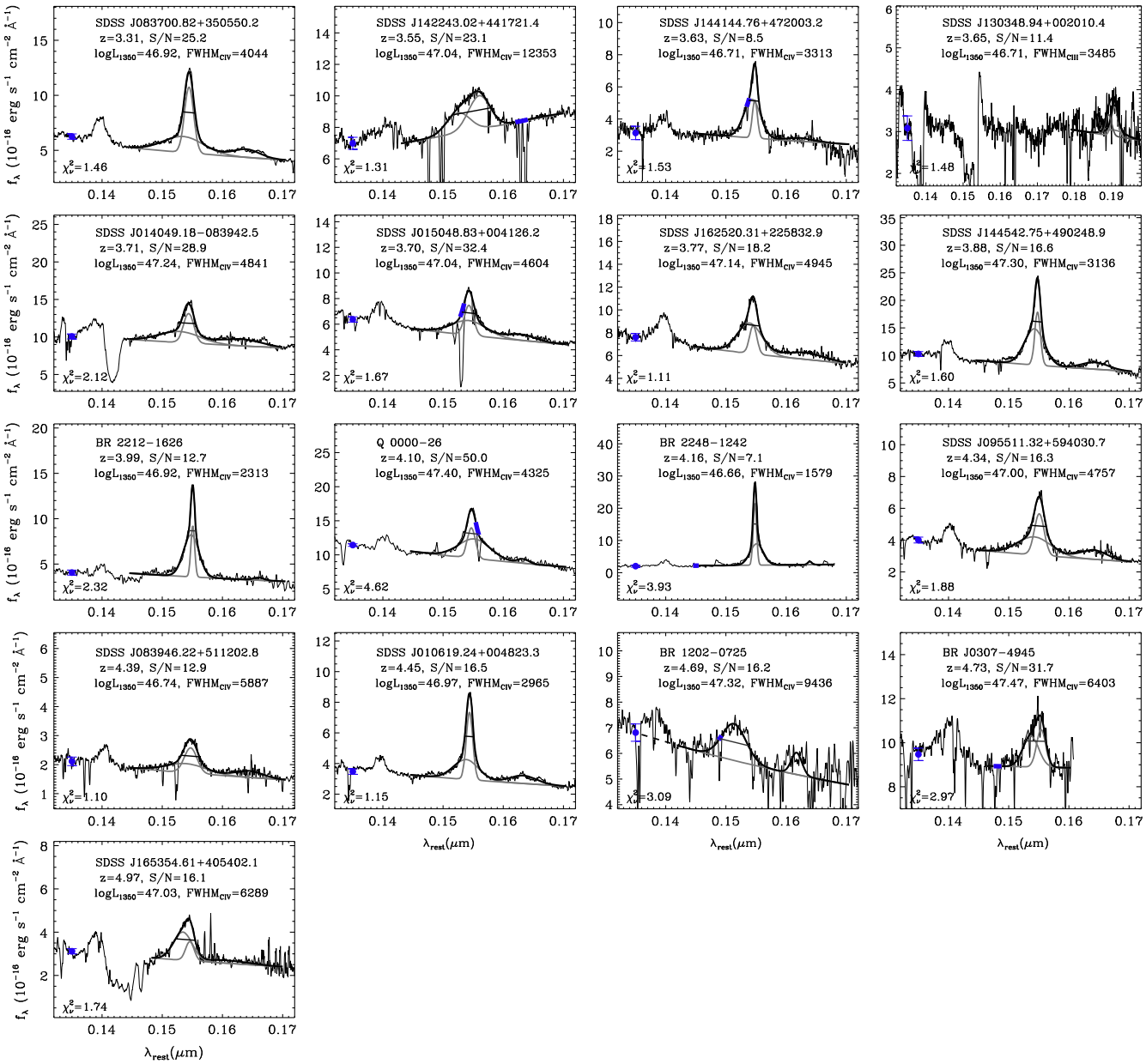

Figure 7. Rest-frame C IV spectral fitting of the identical objects in Figure 6 plotted at the same relative location, following the format of the plotted data and printed numbers. Additionally shown are the double Gaussian fit (gray) to the C IV above the continuum, and the 1350 Å monochromatic flux marked on its wavelength (blue dots), with extrapolated values indicated (dashed lines). The spectra are shown when they are available from the references listed in Table 2. When there were contaminations around the C IV emission, we masked out the region (blue). The C IV spectra displayed are smoothed down to $R = 500$ to highlight the spectral features better.

154 objects observed with NG, 127 are used for the composite construction after removing 27 spectra due to a mild level of confusion from neighbor source spectra, negative continuum levels, or strong fluctuations near the Hα due to warm pixels. The composite is constructed by normalizing the spectra at 5100 Å and taking their error-weighted mean to maximize the S/N. Each spectral flux and error were deredshifted and rebinned to a common wavelength scale of 18 Å per bin, which is equal to that of the *AKARI* at rest-frame Hα. In Figures 10(a)–(c), we plot the composite spectrum and the zoomed-in fit to the Hα and Hβ regions, respectively. The Hα emission is prominent in the composite spectrum, and the spiky feature at 8400 Å is an artifact from a single spectrum with high S/N.

We determine the continuum slope from the 0.5–0.9 μm region from Figure 10(a), where the number of spectra used to construct the composite exceeds 60. The slope $\alpha = -0.52 \pm 0.06$ (where $f_\nu \propto \nu^\alpha$) is close to the $\alpha = -(0.37$–$0.48)$ of Glikman et al. (2006), determined through the composite of local luminous quasars at similar wavelengths, indicating a similarity in the rest-optical continuum shape of luminous type-1 quasars with respect to redshift. Interestingly, we detect a sign of the Hβ emission from Figure 10(c). The Hβ region was fitted with the Boroson & Green (1992) Fe II template, following the method of Shen et al. (2008). We find $L_{\mathrm{H}\alpha}/L_{\mathrm{H}\beta} = 4.5 \pm 1.6$, which is roughly consistent with 3.6 ± 1.4 from luminous $z \sim 2$ quasars (S12) or the model broad Balmer line decrement of AGNs at

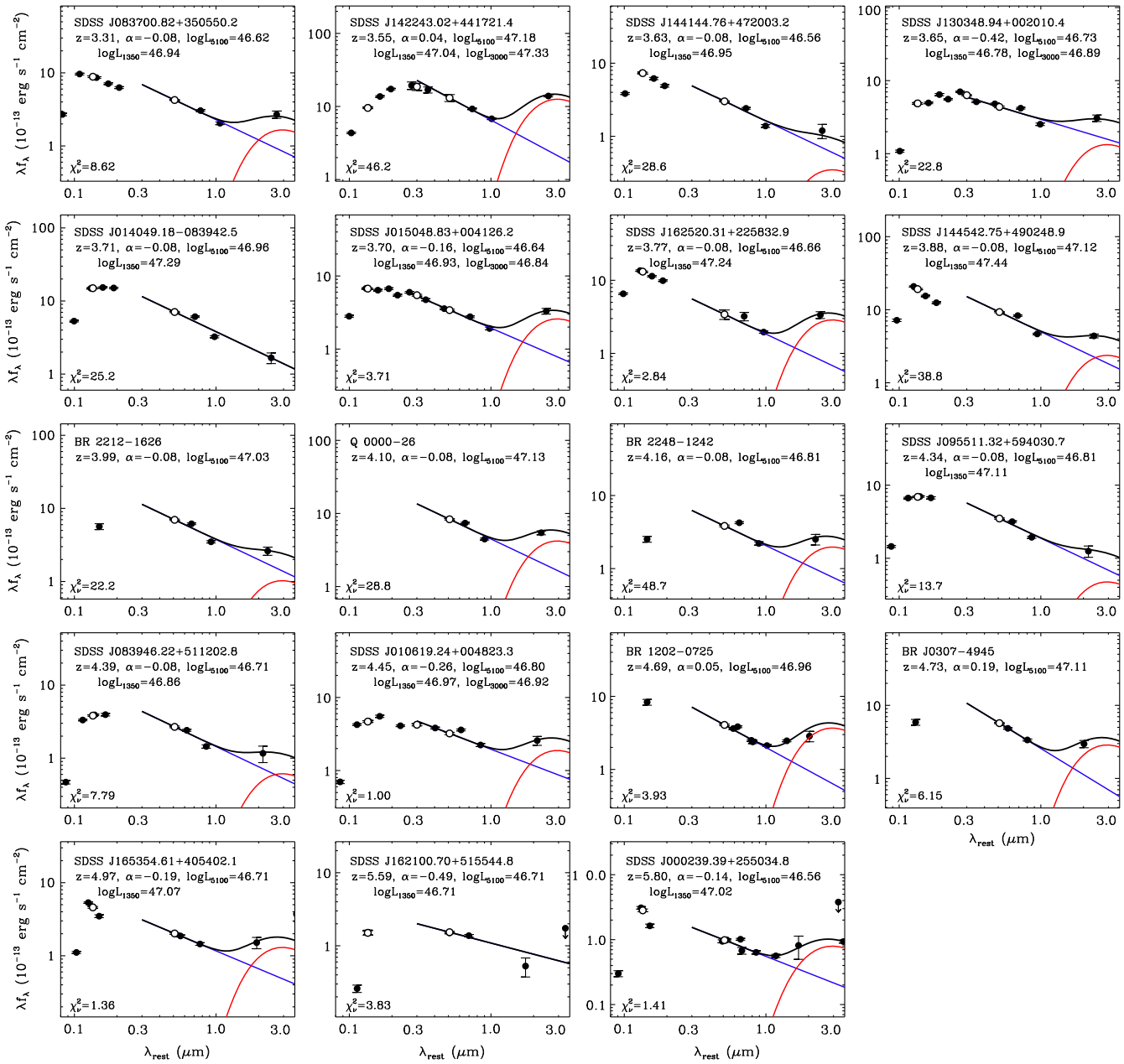

Figure 8. Rest-frame UV–NIR broadband SED of the objects in Figure 6 plotted at the same relative location. The figure shows the observed data points (filled circles) and *WISE* 2σ upper limits (arrows), model fits of the accretion disk (blue line), and the $T = 1250$ K dust components (red curve). Also, the monochromatic 1350, 3000, and 5100 Å fluxes are drawn (open circles) when available.

$T = 10{,}000$–$12{,}000$ K, $L_{H\alpha}/L_{H\beta} = 3.6$–$8.8$ (Osterbrock 1989, p. 422). Because the Balmer decrement value and the $S/N_{H\alpha}$ of each *AKARI* spectrum suggest that the strongest Hβ in our individual spectrum would appear as $S/N_{H\beta} = 1$–2, we do not expect the Hβ emission to be individually detected, consistent with the visual inspection in Section 3.1. Apart from this, we do not find a hint of other emission lines in the composite spectra.

4.2. Luminosity and Line Width Scaling Relations

The derivation of continuum and line luminosities for distant, luminous quasars allows us to examine the universality of the luminosity scaling relations over a wide range of redshifts and luminosities. Starting from the L_{5100}–$L_{H\alpha}$ relation, we plot in Figure 11 our derived data points and the data taken from the literature (Greene & Ho 2005; hereafter G05; Shang et al. 2007; hereafter S07; S11; Ho et al. 2012; Matsuoka et al. 2013; S12) that cover a range of L_{5100} and z, as summarized in Table 4. Our *AKARI* data extend the relation at the high-redshift ($z > 3.3$) and high-luminosity end ($L_{5100} > 10^{46}$ ergs s^{-1}). To minimize the host-galaxy contribution to the AGN luminosities, we chose AGNs with host contamination <20% in L_{5100}, $L_{H\alpha}$ for some data sets (G05; S07), whereas we plotted only the $L_{5100} > 10^{44.73}$ ergs s^{-1} data for the rest of references that meet <10% in host contamination (S11). Meanwhile, the broad $L_{H\alpha}$ could contain the narrow component for *AKARI* data, whereas the broad and narrow line luminosities are combined for the G05, S07, and S11 data too. We find that the contribution from the narrow component

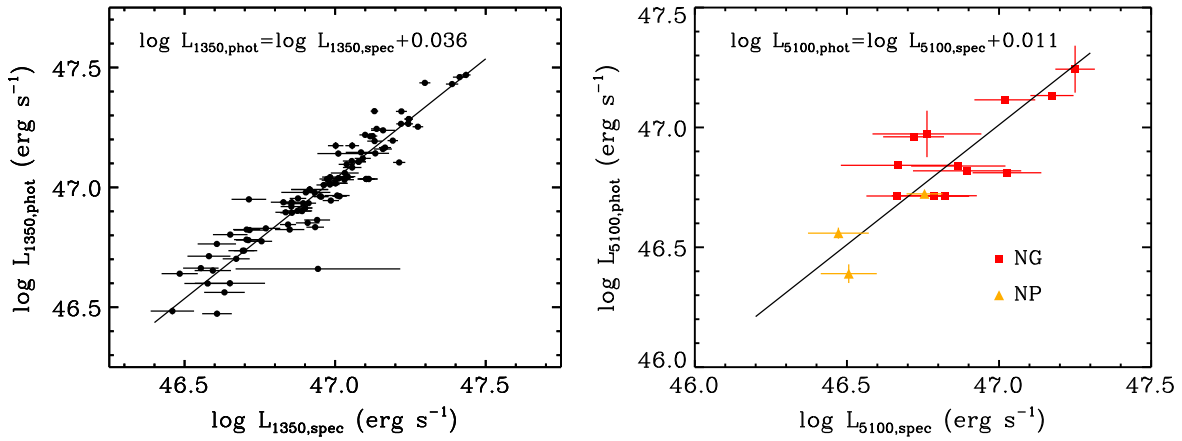

Figure 9. Comparison of spectroscopically and photometrically derived monochromatic luminosities for L_{1350} (left) and L_{5100} (right). The *AKARI* NG and NP data points for the L_{5100} are highlighted with red squares and yellow triangles, respectively. Offsets to the luminosities from a one-to-one relation are displayed.

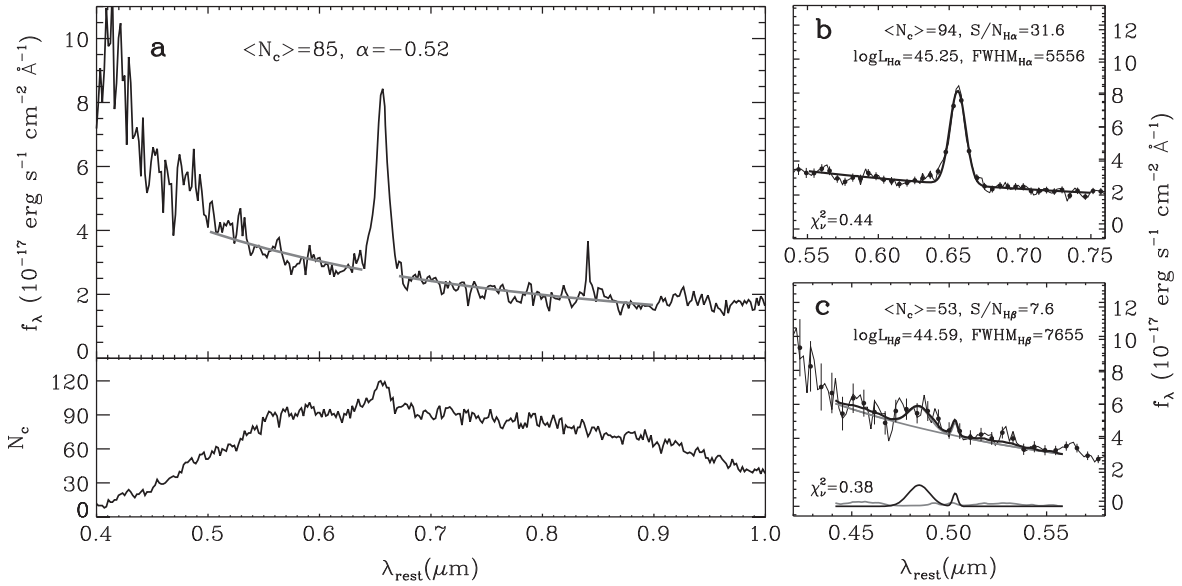

Figure 10. Composite spectra from *AKARI* observations. (a) The spectra within 0.4–1 μm (top), and the number of spectra used to construct the composite, N_c, plotted against wavelength (bottom). The mean N_c and the continuum slope from the 0.5–0.9 μm region are printed. (b) Hα region fit of the composite spectra. (c) Hβ region fit of the composite spectra. The sum of the continuum, Hβ emission, and the Fe II complex (thick black line), and the continuum (gray line) are overplotted on the data, and the Hβ/[O III] and Fe II emission components are separately plotted below the spectrum in black and gray lines.

to $L_{\rm H\alpha}$ estimated from Section 3.1 and the references is negligible (2% and <10%, respectively), allowing us to consider $L_{\rm H\alpha}$ to be approximately the line luminosity of the broad line component.

Figure 11 shows a remarkable correlation between L_{5100} and $L_{\rm H\alpha}$ even when AGNs are drawn from various samples covering a wide range of redshifts and luminosities. This strongly suggests that the physics governing the correlation is the same for low- and high-luminosity AGNs, and there is no strong evolution in the relation from $z=0$ to $z=6$ over the range explored here. The *AKARI* data points are mildly below the relation where the offset could indicate a growing population of weak emission line quasars at high redshift (Fan et al. 1999; Diamond-Stanic et al. 2009), but the overall deviations are within the scatter of the data. The possible downturn in the correlation at very high luminosity (L_{5100} $\sim 10^{47}$ ergs s^{-1}) produces a ~0.2 dex offset in log ($L_{\rm H\alpha}/L_{5100}$), but this downturn affects the $M_{\rm BH}$ estimates only by ~0.1 dex. The possible downturn could be caused by cold accretion disks of slowly spinning, extremely high mass BHs (Laor & Davis 2011; Wang et al. 2014), but we will leave the investigation of the possible downturn as a subject for future work because its effect on the $M_{\rm BH}$ estimates is small. We fitted the relation using the linear regression with bivariate-correlated errors and intrinsic scatter (BCES, Akritas & Bershady 1996)[15] to find the following result:[16]

$$\log L_{\rm H\alpha,42} = \left(1.044 \pm 0.008\right) \log L_{5100,44} + (0.646 \pm 0.011). \quad (2)$$

[15] Throughout this paper we use the BCES fit to derive the linear relations.

[16] Throughout this paper we use subscript numbers on the luminosity to indicate its wavelength and unit, such as $L_{5100,44} = L_{5100\,\text{Å}}/10^{44}$ ergs s^{-1}.

Table 3
Continuum and Line-based Properties of the Sample

Name (1)	$z_{\rm ref}$ (2)	$z_{\rm H\alpha}$ (3)	log L_{1350} (4)	log L_{5100} (5)	log $L_{\rm H\alpha}$ (6)	FWHM$_{3,\rm CIV}$ (7)	FWHM$_{3,\rm H\alpha}$ (8)	log $M_{\rm BH,CIV}$ (9)	log $M_{\rm BH,H\alpha}$ (10)
SDSS J000239.39+255034.8	5.80	5.79	99.00 ± 99.00	46.56 ± 0.02	45.14 ± 0.11	99.00 ± 99.00	2.50 ± −1.00	99.00 ± 99.00	9.25 ± −1.00
Q 0000-26	4.10	4.11	47.40 ± 0.01	47.13 ± 0.01	45.48 ± 0.13	4.33 ± 0.28	2.50 ± −1.00	9.88 ± 0.22	9.56 ± −1.00
SDSS J000552.34–000655.8	5.85	5.85	99.00 ± 99.00	46.04 ± 0.08	44.75 ± 0.32	99.00 ± 99.00	99.00 ± 99.00	99.00 ± 99.00	99.00 ± 99.00
BR J0006–6208	4.45	4.49	46.90 ± 0.02	46.71 ± 0.00	45.46 ± 0.06	11.33 ± 1.33	2.85 ± 0.85	10.48 ± 0.24	9.46 ± 0.31
SDSS J001115.23+144601.8	4.97	99.00	99.00 ± 99.00	46.78 ± 0.02	47.97 ± −1.00	99.00 ± 99.00	99.00 ± 99.00	99.00 ± 99.00	99.00 ± 99.00

Note. Catalog of the properties derived for the *AKARI* quasars, sorted by right ascension. Column 1: target name; Column 2: redshift from references; Column 3: redshift measured from Hα; Column 4: 1350 Å luminosity and its uncertainty; Column 5: 5100 Å luminosity and its uncertainty; Column 6: Hα luminosity and its uncertainty; Column 7: FWHM of the C IV line and its uncertainty; Column 8: FWHM of the Hα line and its uncertainty; Column 9: $M_{\rm BH}$ from the C IV line and its uncertainty; Column 10: $M_{\rm BH}$ from the Hα line and its uncertainty. The units for L, FWHM, and $M_{\rm BH}$ are ergs s^{-1}, 1000 km s^{-1}, and $M_\odot$. Columns 9 and 10 are from Equations (10) and (7), respectively. Empty parameters are entered as 99 and upper limits are given with errors of −1.

(This table is available in its entirety in machine-readable form.)

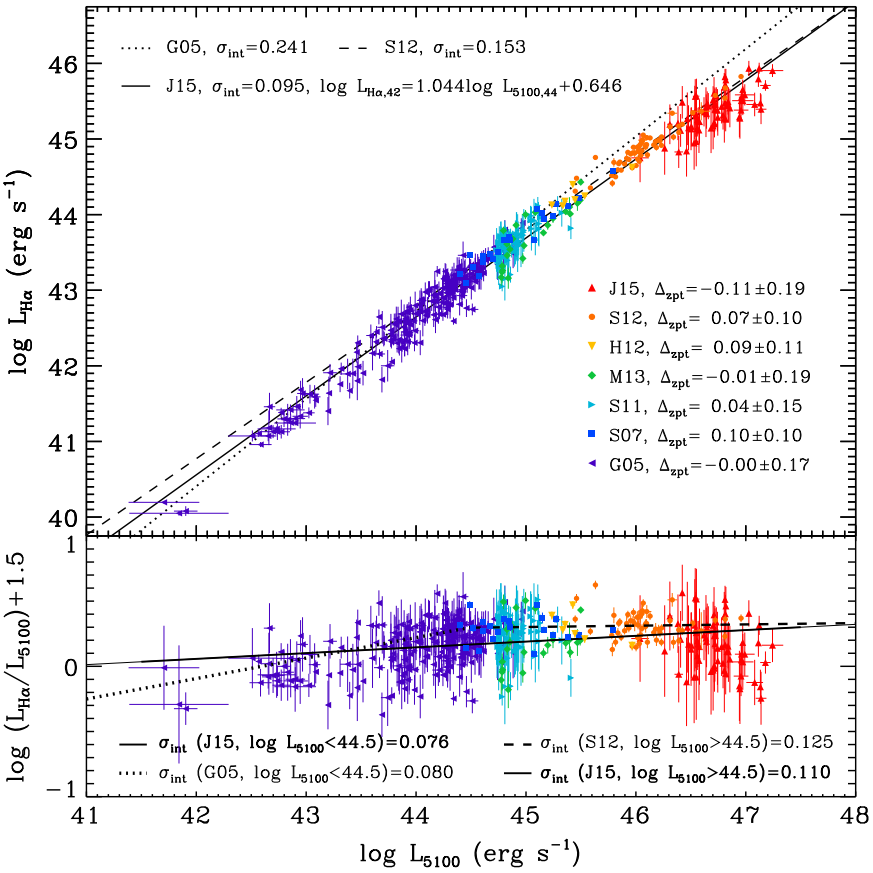

Figure 11. L_{5100}–$L_{\rm H\alpha}$ relation of AGNs (top), and its projection on the L_{5100}–$L_{\rm H\alpha}/L_{5100}$ (bottom), from the combined references. The references abbreviated on the plot are summarized in Table 4, where all measurements from references are converted to our adopted cosmology. We limited the G05 data to $L_{5100} < 10^{44.73}$ ergs s^{-1} to avoid overlap with the S11 data. The L_{5100}–$L_{\rm H\alpha}$ relation from G05, S12, and J15 is shown as dotted, dashed, and solid lines, respectively. The zero-point offset and rms scatter of each literature data point with respect to our relation are denoted as $\Delta_{\rm zpt}$. The intrinsic scatter ($\sigma_{\rm int}$, dex) of the entire data set with respect to the G05, S12, and J15 relations (top), and of the data divided by $L_{5100} = 10^{44.5}$ ergs s^{-1} (bottom), are shown. The L_{5100} in M13 and J15 are from photometric SED fitting (Section 3.2), and the rest are spectroscopically derived from each reference. The $L_{\rm H\alpha}$ are from broad emission for all references but for the G05, S07, and S11 data, where the narrow component is included.

The best-fit relation fits the entire data with $\sigma_{\rm int} = 0.095$ dex. The flux–flux relation of the 5100 Å continuum and Hα shows almost identical slope and intrinsic scatter, suggesting that the tight correlation in Equation (2) is not due to a sample selection effect. The data points at three redshift intervals, namely $0 < z < 0.8$ (G05, S07, and S11) for $41.7 < \log L_{5100} < 46.4$, $0.7 < z < 2.2$ for $44.8 < \log L_{5100} < 47.0$ (H12, S12, and M13), and $3.3 < z < 6.2$ for $46.0 < \log L_{5100} < 47.2$ (J15), overlap each other and show no evolution. This suggests that Equation (2) is universal and not due to a distance effect like the Malmquist bias.

To examine the universality of the relation further, we discuss how the L_{5100}–$L_{\rm H\alpha}$ relation of G05 at $z \sim 0$ of lower luminosity AGNs and S12 at $z \sim 2$ of higher luminosity AGNs

Table 4
Dynamic Range of References

Reference	z	log L_{5100} (ergs s^{-1})
G05	<0.35	41.7–45.0
N07	2.3–3.5	45.2–46.3
S07	0.08–0.40	44.4–45.8
M08	0.35–0.37	43.6–44.4
D09	1.1–2.2	46.1–46.7
W09	0.00–0.16	42.0-45.9
A11	1.4–3.6	44.8-46.5
S11	0.08–0.80	43.8–46.4
H12	1.4–1.5	45.2–46.0
S12	1.5–2.2	45.4–47.0
B13	0.00–0.29	42.0–45.9
M13	0.7–1.7	44.8–45.5
P13	0.01–0.23	42.6–45.9
J15	3.3–6.2	46.0–47.2

Note. The abbreviated references are Greene & Ho 2005 (G05), Netzer et al. 2007 (N07), Shang et al. 2007 (S07), McGill et al. 2008 (M08), Dietrich et al. 2009 (D09), Wang et al. 2009 (W09), Assef et al. 2011 (A11), Shen et al. 2011 (S11), Ho et al. 2012 (H12), Shen & Liu 2012 (S12), Bentz et al. 2013 (B13), Matsuoka et al. 2013 (M13), Park et al. 2013 (P13), and this work (J15).

fare with each literature value. First, the G05 relation can describe the L_{5100}–$L_{H\alpha}$ relation of S07, S11, and M13 AGNs over the overlapping luminosity interval ($L_{5100} \lesssim 10^{45}$ ergs s^{-1}). When extrapolated to higher luminosity, it starts to deviate from the data points regardless of redshift. Likewise, the S12 relation can describe the L_{5100}–$L_{H\alpha}$ relation down to $L_{5100} \lesssim 10^{44.5}$ ergs s^{-1}, including the S07 data at $z < 0.4$ and our AGNs at $z > 3.3$. However, when applied to the entire data sets, the G05 and S12 relations show deviations from the data at high- and low-luminosity regions, respectively. Consequently, both relations produce $\sigma_{\rm int} = 0.15$–0.24 dex against the data, which is worse than the 0.095 dex of our L_{5100}–$L_{H\alpha}$ relation.

To check if the inconsistency in the G05 and S12 relations at the faint and luminous end arises from a possible break in the relation itself, we considered the case where the slope changes at $L_{5100} \sim 10^{44.5}$ ergs s^{-1}, where the G05 and S12 relations meet. For this, we computed the $\sigma_{\rm int}$ of the $L_{5100} < 10^{44.5}$ ergs s^{-1} and $L_{5100} > 10^{44.5}$ ergs s^{-1} data against the G05, S12, and our relation in Equation (2), and we examined whether our simple relation is any worse than the combination of the G05 and S12 relations with a break at $L_{5100} = 10^{44.5}$ ergs s^{-1}. As indicated in the lower panel of Figure 11, the $\sigma_{\rm int}$ values against our relation are comparable to or slightly smaller than the $\sigma_{\rm int}$ against the G05 or S12 relations at low and high luminosities, respectively. This suggests that there is no strong need for a broken power-law form of the L_{5100}–$L_{H\alpha}$ relation, and a simple relation of Equation (2) can be employed to describe the response of BLR to the incident continuum emission over the covered redshift and luminosity ranges in Figure 11 and Table 4.

Likewise, we plot in Figure 12 the L_{5100}–L_{1350} and L_{5100}–L_{3000} relations from the luminosities derived in Section 3 and taken from the references. Apart from the literature data where the host contamination in L_{5100} is estimated to be <20% (S07) or minimized by *Hubble Space Telescope* (*HST*) observations, we limit the literature sample with $L_{5100} > 10^{44.73}$ ergs s^{-1} to keep the host galaxy contamination below 10% (S11). Meanwhile, we replaced the L_{5100} of Wang et al. (2009) and Park et al. (2013) with the *HST* data from Bentz et al. (2013), while only including the AGNs with <20% host contamination in L_{5100}. Similar to the L_{5100}–$L_{H\alpha}$ relation, we do not find any evolution in the L_{5100}–L_{1350} and L_{5100}–L_{3000} relations for a particular set of data, and we find the best-fit correlation to be

$$\begin{aligned}\log L_{1350,44} &= \left(0.974 \pm 0.023\right) \log L_{5100,44} \\ &\quad + (0.391 \pm 0.053) \\ \log L_{3000,44} &= \left(0.973 \pm 0.010\right) \log L_{5100,44} \\ &\quad + (0.287 \pm 0.013). \end{aligned} \quad (3)$$

The $\sigma_{\rm int}$ values (dex) to these best-fit relations, as well as the relation with respect to S12, are presented in Figure 12. Like for the $L_{H\alpha}$–L_{5100} relation, the flux–flux relations show slopes and intrinsic scatter that are virtually identical to the luminosity–luminosity relations, showing again that the sample selection effect is not a main driver for the relations in Equation (3).

Finally, we compare the broad line FWHM of Hβ, Hα, Mg II, and C IV in Figure 13 in order to calibrate the $M_{\rm BH}$ from multiple line-based recipes and to check for any evolution in the FWHM relations. For a good comparison of FWHMs, we restricted the mixed samples to have the fractional errors of FWHM less than 20%, while additionally limiting the S/N and reduced chi-square of the SDSS spectra to be S/N > 20 and $\chi^2_\nu < 2$. In Figure 13(a), we fit the FWHM$_{H\beta}$–FWHM$_{H\alpha}$ relation from the collected data, where we find the offset of each reference data point to this relation to fall within each scatter. The $\sigma_{\rm int}$ of all of the data to our relation, 0.063 dex, is smaller than when using the relation from G05.

Second, we derive the FWHM$_{H\beta}$–FWHM$_{Mg_{II}}$ relation. Because it is debatable whether to subtract the narrow component for the Mg ii line width measurement (e.g., S11), we followed Jun & Im (2013) to average the FWHM$_{Mg_{II}}$ derived with and without the subtraction of the narrow component. Also, the slope and constant of the relation are consistent within uncertainty with those derived with and without the subtraction of the narrow FWHM$_{Mg_{II}}$ component. Therefore, we combined the literature data with respective treatment of the narrow Mg II and the averaged FWHM$_{Mg_{II}}$ in S11, to derive the FWHM$_{H\beta}$–FWHM$_{Mg_{II}}$ relation altogether. We note that the relative FWHM offset of the literature data to our relation shown in Figure 13(b) is within the scatter of data points, indicating that the details of fitting to exclude the narrow Mg II component (S07; McGill et al. 2008; Dietrich et al. 2009) or to include but subtract it (Wang et al. 2009; S12) do not affect the line widths significantly when compared overall. The rms of all of the data to our relation, 0.085 dex, is similar to that from Wang et al. (2009) and small enough to regard the FWHM$_{Mg_{II}}$ as a marginally good substitute for FWHM$_{H\beta}$ as much as FWHM$_{H\alpha}$.

Third, we derive the FWHM$_{H\beta}$–FWHM$_{C_{IV}}$ relation in Figure 13(c). The data can be fitted altogether with a log-linear relation, but the $\sigma_{\rm int}$ of the data to the relation, 0.212 dex, is large and comparable to the systematic uncertainty of single-

Table 5
L_{5100}–$L_{H\alpha}$ Relation

Reference (1)	α (2)	β (3)	σ_{int} (4)	$\sigma_{int,\ all}$ (5)	N (6)	z (7)	log L_{5100} (8)	Dataset (9)
Greene & Ho (2005)	0.720 ± 0.002	1.157 ± 0.005	0.078	0.241	229	<0.35	41.7-45.0	G05
Shen & Liu (2012)	0.791 ± 0.093	1.010 ± 0.042	0.088	0.153	60	1.5-2.2	45.4-47.0	S12
This work	0.646 ± 0.011	1.044 ± 0.008	0.095	0.095	464	0.0–6.2	41.7-47.2	G05, S07, S11, H12, S12, M13, J15

Note. The L_{5100}–$L_{H\alpha}$ relations from previous studies and this work, where α and β are defined as log $L_{H\alpha,42} = \alpha + \beta$ log $L_{5100,44}$. Column 1: reference; Column 2: α and its uncertainty (1σ); Column 3: β and its uncertainty; Column 4: intrinsic scatter (dex) of the relation over the L_{5100} range covered; Column 5: intrinsic scatter of the relation over the range $41.7 <$ log $L_{5100} < 47.2$; Column 6: number of objects used; Column 7: redshift range; Column 8: range of L_{5100} (ergs s^{-1}); Column 9: references of the AGN data set with abbreviations from Table 4.

Table 6
Virial Mass Estimators

Reference (1)	α (2)	β (3)	γ (4)	N (5)	z (6)	log M_{BH} (7)	Method (8)
M_{BH} ($L_{5100,44}$, FWHM$_{H\beta,3}$)							
Greene & Ho (2005)	6.64 ± 0.02	0.64 ± 0.02	2	35	<0.37	5.5–9.0	RM
Vestergaard & Peterson (2006)	6.91 ± 0.02	0.5	2	25	0.00–0.29	7.2–9.3	RM
Bentz et al. (2013), this work	6.94 ± 0.12	0.533 ± 0.034	2	41	0.00–0.29	6.0–10.7	RM
M_{BH} ($L_{5100,44}$, FWHM$_{H\alpha,3}$)							
Greene & Ho (2005)	6.70 ± 0.06	0.64 ± 0.02	2.06 ± 0.06	162	<0.37	5.2–9.0	SE
Shen & Liu (2012)	7.01	0.555	1.87	60	1.5–2.2	8.8–10.3	SE
This work	7.05 ± 0.12	0.533 ± 0.034	2.12 ± 0.03	654	0.0–2.4	5.8–10.6	SE
M_{BH} ($L_{H\alpha,42}$, FWHM$_{H\alpha,3}$)							
Greene & Ho (2005)	6.30 ± 0.08	0.55 ± 0.02	2.06 ± 0.06	243	<0.37	5.1–9.0	SE
Shen & Liu (2012)	6.55	0.564	1.82	60	1.5–2.2	8.8–10.2	SE
This work	6.72 ± 0.12	0.511 ± 0.033	2.12 ± 0.03	969	0.0–6.2	5.6–10.5	SE
M_{BH} ($L_{3000,44}$, FWHM$_{MgII,3}$)							
McLure & Dunlop (2004)	6.5	0.62	2	22	0.03–0.37	7.5–8.9	RM
Vestergaard & Osmer (2009)	6.86	0.5	2	...	...	...	SE
Wang et al. (2009)	7.15 ± 0.27	0.46 ± 0.08	1.48 ± 0.49	29	0.00–0.16	6.3–9.0	RM
Shen & Liu (2012)	6.95	0.584	1.71	60	1.5–2.2	8.8–10.1	SE
This work	6.62 ± 0.12	0.548 ± 0.035	2.45 ± 0.06	1010	0.0–6.4	6.8–10.3	SE
M_{BH} ($L_{1350,44}$, FWHM$_{CIV,3}$)							
Vestergaard & Peterson (2006)	6.66 ± 0.01	0.53	2	27	0.00–0.23	5.5–9.3	RM
Shen & Liu (2012)	8.02	0.471	0.24	60	1.5–2.2	8.9–9.6	SE
Park et al. (2013)	7.48 ± 0.24	0.52 ± 0.09	0.56 ± 0.48	25	0.01–0.23	7.0–9.0	RM
This work	6.67 ± 0.15	0.547 ± 0.037	2.11 ± 0.11	258	0.0–5.4	6.8–10.7	SE

Note. The M_{BH} relations from previous studies and this work, where α, β, and γ are defined as log $M_{BH} = \alpha + \beta$ log $L + \gamma$ log FWHM. Column 1: reference; Column 2: α and its uncertainty (1σ); Column 3: β and its uncertainty; Column 4: γ and its uncertainty; Column 5: number of objects used for luminosity or line width calibration; Column 6: redshift range of objects used for luminosity or line width calibration; Column 7: range of M_{BH} from reference; Column 8: method of calibration, where RM and SE denote calibrations of the luminosity and line width using the reverberation-mapped and single-epoch samples, respectively.

epoch M_{BH} estimators when scaled as the FWHM squared. We checked the effect of the fitting methodology by deriving all of the L–L and FWHM–FWHM relations with the FITEXY method (Tremaine et al. 2002) to find that the slope of the FWHM$_{H\beta}$–FWHM$_{C_{IV}}$ relation, 1.798 ± 0.026, shows a meaningfully large difference from the BCES results. Still, we keep the BCES slope because it makes the Balmer and C IV M_{BH} estimates more consistent (Section 4.3), and we note that the large σ_{int} in the FWHM$_{H\beta}$–FWHM$_{C_{IV}}$ relation represents a poor correlation at best.

Overall, we find the relations of FWHM$_{H\alpha}$, FWHM$_{Mg_{II}}$, and FWHM$_{C_{IV}}$ against the FWHM$_{H\beta}$ without any noticeable evolution for the samples considered, covering a wide range of luminosity or redshift. Therefore, although the data for calibration are missing at $z \gtrsim 3$, we use our FWHM relations to calibrate the M_{BH} estimators for general usage

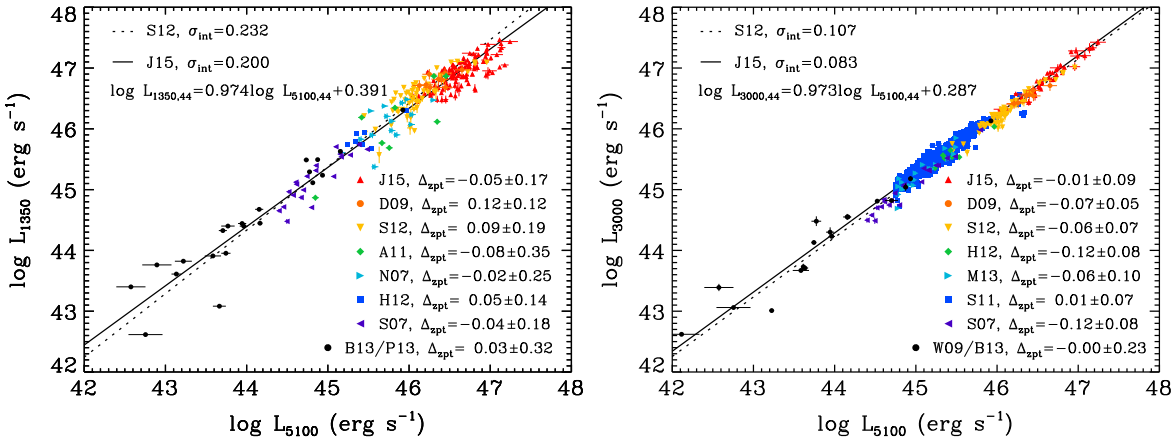

Figure 12. L_{5100}–L_{1350} and L_{5100}–L_{3000} relations of AGNs from the combined references. The references abbreviated on the plot are summarized in Table 4, where all measurements from the references are converted to our adopted cosmology. The L_{1350} of the N07 sample are searched from S11. The L_{5100}, L_{3000}, and L_{1350} are derived from spectra, except for the L_{5100} and L_{3000} from J15, where they are from photometric SED fitting (Section 3.2). We assign a modest 10% error for L_{5100} of the N07 data and L_{1350}, L_{5100} of the A11 data, and a 20% error for the L_{1350}, L_{3000}, and L_{5100} from the D09 data, from visual inspection of their spectra. We removed the highly variable object 3C 390.3 from the B13 data, and an additional two objects in the S07 data that overlap with B13. The L_{5100}–L_{1350} and L_{5100}–L_{3000} relations from S12 and J15 are shown as dotted and solid lines, respectively. The zero-point offset and rms scatter of each literature data point with respect to our relations are indicated.

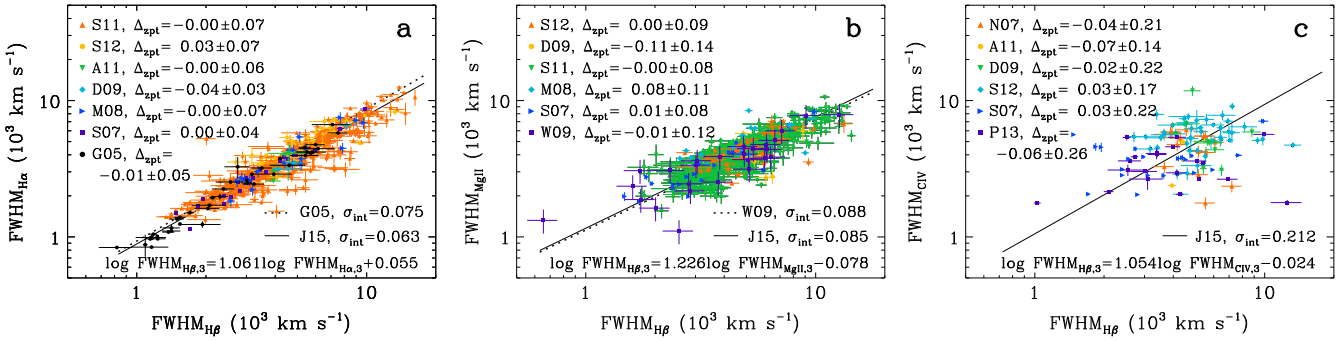

Figure 13. FWHM$_{H\beta}$–FWHM$_{H\alpha}$, FWHM$_{H\beta}$–FWHM$_{MgII}$, and FWHM$_{H\beta}$–FWHM$_{CIV}$ relations of AGNs from the combined references. The references abbreviated on the plot are summarized in Table 4. The *AKARI* data are not present because the samples do not have simultaneous coverage of the FWHMs plotted. We limited the G05 data to $L_{5100} < 10^{43.83}$ ergs s^{-1} to avoid overlap with the S11 data. We assign a 10% error for the FWHM$_{H\beta}$ and FWHM$_{CIV}$ of the N07 data, following their argument. We removed one object in the S07 data that overlaps with W09, and two objects in S07 that overlap with P13. The FWHM$_{H\beta}$–FWHM$_{H\alpha}$ relation of G05 and the FWHM$_{H\beta}$–FWHM$_{MgII}$ relation of W09 are shown as dotted lines, and the relations from this work are shown as solid lines. The zero-point offset and rms scatter of each literature data point with respect to our relations are indicated. The FWHMs are of the broad emission line.

in terms of redshift. Our derived FWHM relations are as follows:[17]

$$\begin{aligned}&\log \mathrm{FWHM}_{H\beta,3}\\ &= \left(1.061 \pm 0.013\right) \log \mathrm{FWHM}_{H\alpha,3} + \left(0.055 \pm 0.008\right)\\ &= \left(1.226 \pm 0.032\right) \log \mathrm{FWHM}_{Mg_{II},3} - \left(0.078 \pm 0.021\right)\\ &= \left(1.054 \pm 0.057\right) \log \mathrm{FWHM}_{C_{IV},3} - \left(0.024 \pm 0.045\right).\end{aligned} \quad (4)$$

We note the possibility that the FWHM relations established with spectra taken in different epochs could be affected by variability of the emission line shape, especially when the dynamic range of the probed FWHMs are narrower than that of the continuum luminosities. Still, the offset or scatter of the references with and without simultaneously acquired data in Figure 13 do not differ from each other. Also, we find the average and rms scatter in the ratio of the SDSS-III BOSS over SDSS-I/SDSS-II FWHM$_{C_{IV}}$ from 12, S/N > 15 objects matched with the *AKARI* sample to be 0.99 ± 0.08, which implies that the effect of variability to the shift or broadening of the FWHM$_{H\beta}$–FWHM$_{C_{IV}}$ relation is negligible compared to the σ_{int} of the relation by an order of magnitude.

4.3. Updated M_{BH} Estimators

Using the scaling relations obtained above, we now present an updated set of M_{BH} estimators based on various lines. Because the reverberation mapping of Hβ and L_{5100} forms the basis of mass estimation for AGNs, we start from the M_{BH} estimator that uses the 5100 Å luminosity and Hβ line width to take the following form and derive other estimators using the

[17] Throughout this paper we use subscript numbers on the line width to indicate its unit, such as FWHM$_{H\beta,3}$ = FWHM$_{H\beta}$/10^3 km s^{-1}.

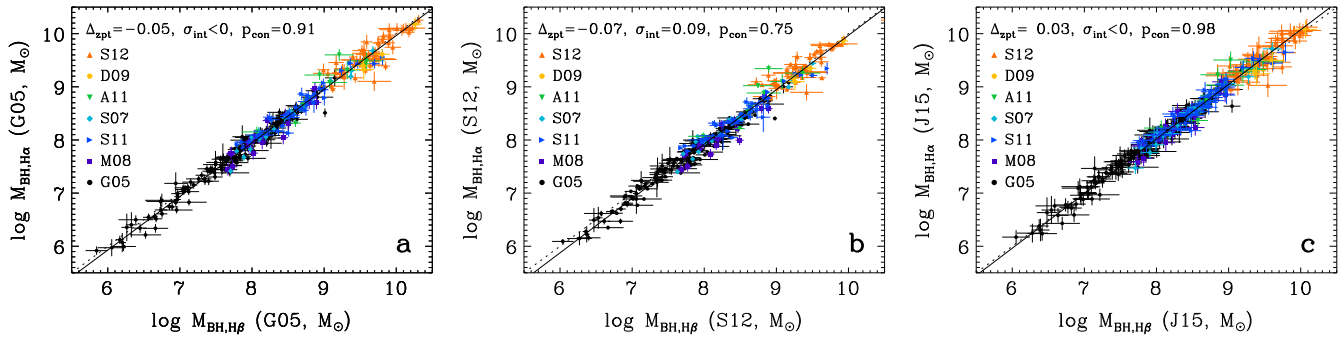

Figure 14. Comparison of Balmer $M_{\rm BH}$ relations of AGNs from the combined references. The references abbreviated on the plot are summarized in Table 4. All measurements are converted to our adopted cosmology and f factor. We limited the G05 data to $L_{5100} < 10^{44.73}$ ergs s^{-1} and the S11 data to $L_{5100} > 10^{44.73}$ ergs s^{-1} in order to avoid overlap. The linear fit to the $M_{\rm BH}$ relation and a one-to-one relation are represented by solid and dotted lines, respectively, whereas the zero-point offset between the masses ($\Delta_{\rm zpt}$) intrinsic scatter with respect to a one-to-one relation ($\sigma_{\rm int}$, dex) and the fraction where the masses overlap within error ($P_{\rm con}$) are printed.

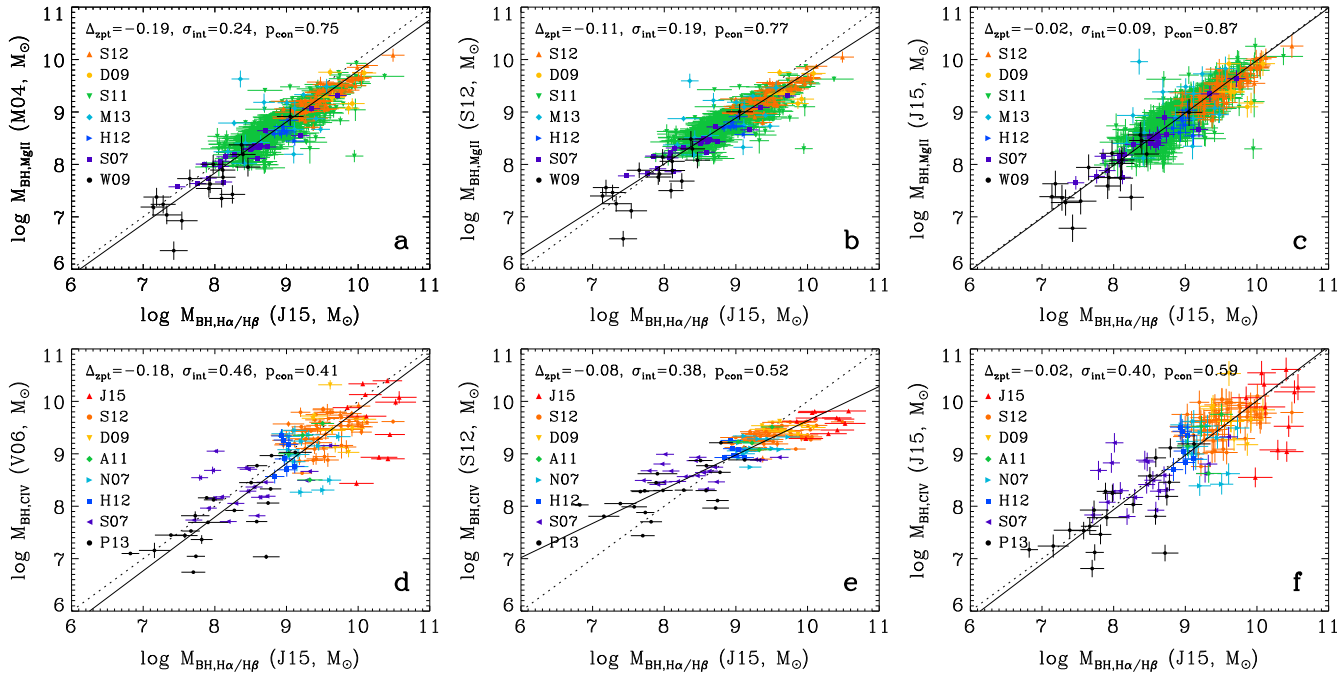

Figure 15. Comparison of Balmer $M_{\rm BH}$ to the UV $M_{\rm BH}$ of AGNs from combined references. The references abbreviated on the plot are summarized in Table 4, with M04, V06 estimators from McLure & Dunlop (2004) and Vestergaard & Peterson (2006). All measurements are converted to our adopted cosmology and f factor. We use the $M_{\rm BH}(L_{5100}, {\rm FWHM_{H\alpha}})$ for the Balmer masses, unless when the Hα line was uncovered and the $M_{\rm BH}(L_{5100}, {\rm FWHM_{H\beta}})$ was used. The rest of the figure format follows that of Figure 14. We removed the objects unused in Figures 13 and 14.

scaling relations discussed above:

$$M_{\rm BH} = \frac{f}{G} R_{\rm BLR}(L_{5100}) \left(\frac{{\rm FWHM_{H\beta}}}{2} \right)^2 . \quad (5)$$

Previous secondary calibrations to the $M_{\rm BH}$ were performed by replacing the (L_{5100}, FWHM$_{\rm H\beta}$) of the local reverberation-mapped sample or SDSS AGNs by ($L_{\rm H\alpha}$, FWHM$_{\rm H\alpha}$) (e.g., Greene & Ho 2005), (L_{3000}, FWHM$_{\rm MgII}$) (e.g., McLure & Jarvis 2002), or (L_{1350}, FWHM$_{\rm C_{IV}}$) (e.g., Vestergaard & Peterson 2006). Using the latest R–L relation from Bentz et al. (2013)[18] and the constant for the mass equation (f factor, $f = 5.1 \pm 1.3$) from Woo et al. (2013), we first derive the Hβ $M_{\rm BH}$ estimator as

$$R_{\rm BLR} = \left(34.7 \pm 2.5\right) L_{5100,44}{}^{(0.533\pm0.034)} \ {\rm lt-day}$$
$$M_{\rm BH}\left(L_{5100}, {\rm FWHM_{H\beta}}\right) = \left(8.63 \pm 2.29\right) \times 10^6 \times L_{5100,44}{}^{(0.533\pm0.034)} \, {\rm FWHM_{H\beta,3}}{}^2 \, M_\odot . \quad (6)$$

Replacing the Hβ line width through the FWHM$_{\rm H\beta}$–FWHM$_{\rm H\alpha}$ relation from Equation (4), we get the $M_{\rm BH}$ from (L_{5100}, FWHM$_{\rm H\alpha}$):

$$M_{\rm BH}\left(L_{5100}, {\rm FWHM_{H\alpha}}\right) = (1.11 \pm 0.30) \times 10^7 \times L_{5100,44}{}^{(0.533\pm0.034)} \, {\rm FWHM_{H\alpha,3}}{}^{(2.12\pm0.03)} \, M_\odot . \quad (7)$$

[18] We shifted the relation to the Hubble parameter of $H_0 = 70$ km s^{-1} Mpc^{-1}, which is our adopted value throughout this work.

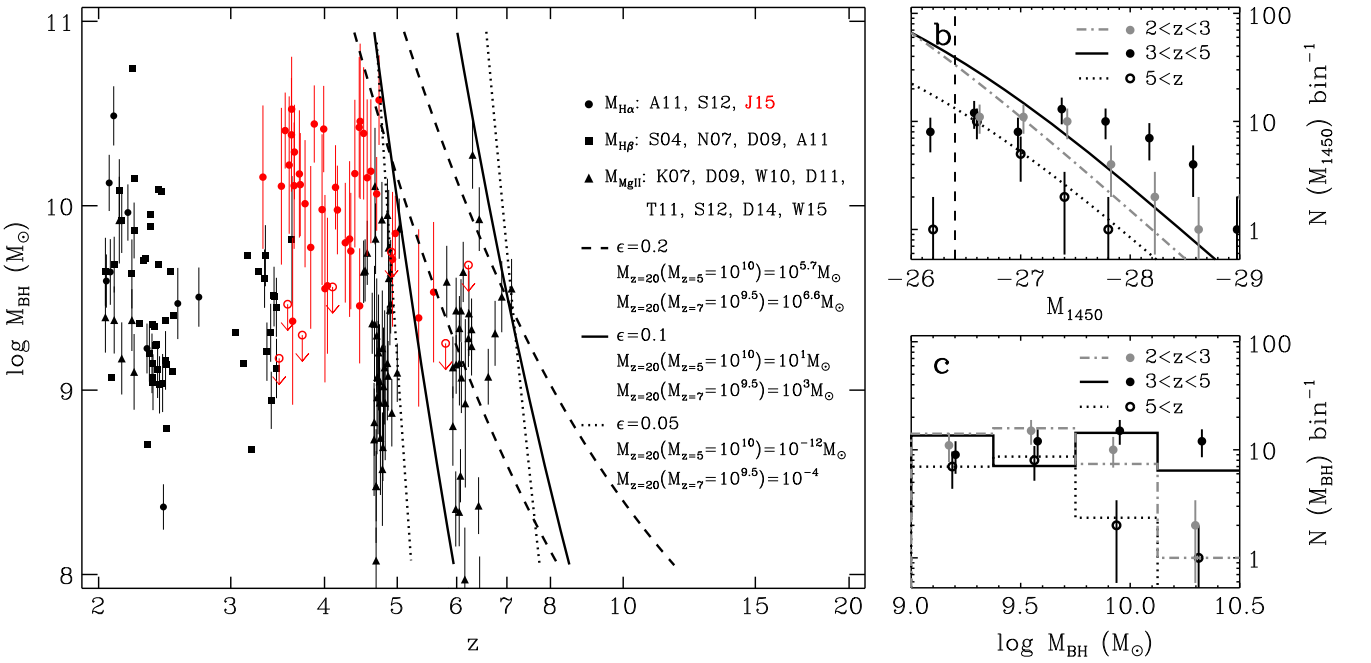

Figure 16. $M_{\rm BH}$ of AGNs along redshift (left). The $M_{\rm BH}$ from Hα are in circles, Hβ in squares, and Mg II in triangles, and our *AKARI* data points are in red circles. For objects with multiple lines, we choose the Hα over Hβ, and Hβ over Mg II, and for repeated measurements of an object we used the latest results. Most of the references abbreviated on the plot are summarized in Table 4, with S04, K07, W10, D11, T11, D14, and W15 additionally from Shemmer et al. (2004), Kurk et al. (2007), Willott et al. (2010a), De Rosa et al. (2011), Trakhtenbrot et al. (2011), De Rosa et al. (2014), and Wu et al. (2015), respectively. We do not plot the error for the S04 data because they are not available, and we do not use a part of the T11 data with poor quality (flagged "3"). The model tracks of exponential BH growth that match the massive envelope of AGNs at $z \sim 5$ and 7 are plotted, with each set of parameters describing the curve shown. On the right, we plot the histogram of M_{1450} (top) and $M_{\rm BH}$ (bottom) at each denoted redshift bin in circles, with errors determined through Poisson statistics. The luminosity functions scaled to the observed number counts to yield the same number at $M_{1450} < -26.4$ at each redshift (top), and the resultant mass counts from the luminosity scaling and a FWHM > 2500 km s^{-1} cut (bottom), are overplotted in lines with styles marked next to the redshift.

Finally, the application of Equation (2) yields the $M_{\rm BH}$ from ($L_{\rm H\alpha}$, FWHM$_{\rm H\alpha}$):

$$M_{\rm BH}\left(L_{\rm H\alpha}, {\rm FWHM}_{\rm H\alpha}\right) = (5.20 \pm 1.41) \times 10^6 \times L_{\rm H\alpha,42}{}^{(0.511\pm0.033)}\, {\rm FWHM}_{\rm H\alpha,3}{}^{(2.12\pm0.03)}\, M_\odot. \quad (8)$$

Likewise, replacing the continuum luminosity and line width in Equation (6) with those of Mg II and C IV using Equations (3) and (4) yields

$$M_{\rm BH}\left(L_{3000}, {\rm FWHM}_{\rm Mg_{II}}\right) = \left(4.19 \pm 1.19\right) \times 10^6 \times L_{3000,44}{}^{(0.548\pm0.035)}\, {\rm FWHM}_{\rm Mg_{II},3}{}^{(2.45\pm0.06)}\, M_\odot \quad (9)$$

$$M_{\rm BH}\left(L_{1350}, {\rm FWHM}_{\rm C_{IV}}\right) = \left(4.72 \pm 1.63\right) \times 10^6 \times L_{1350,44}{}^{(0.547\pm0.037)}\, {\rm FWHM}_{\rm C_{IV},3}{}^{(2.11\pm0.11)}\, M_\odot. \quad (10)$$

The $M_{\rm BH}$s based on Hα and C IV from our estimators for the *AKARI* sample are given in Table 3. It is worth noting that Equation (5) may not hold if the FWHM$_{\rm H\beta}$ is not exactly proportional to the velocity dispersion, σ (Peterson et al. 2004; Collin et al. 2006), or if the *R–L* relation breaks down at high luminosity where the relation has not been tested extensively with the reverberation technique ($L_{5100} > 10^{46}$ ergs s^{-1}, Bentz et al. 2013). Nevertheless, considering the advantages of using the FWHM (to be robust under poor sensitivity, wings in the line profile, or deblending; see S12) for the single-epoch mass estimation, and the current expectations in the high-luminosity *R–L* relation (see Section 5.1), our set of calibrations has the merit where the rest-UV to optical $M_{\rm BH}$ estimations are mutually consistent through a wide range of redshifts, luminosities, and fitting methodologies.

To check the consistency between our $M_{\rm BH}$ estimators, we first compare the Balmer $M_{\rm BH}$ using the estimator in this work and existing estimators in Figure 14. The $M_{\rm BH,H\beta}$ and $M_{\rm BH,H\alpha}$ are compared, where a $\Delta M_{\rm BH} < 0.3$ dex error cut is applied to the data out of various references. The $M_{\rm BH}$ values are derived from the G05, S11 estimators and from this work (Equations (6) and (7) in Figures 14(a)–(c)), respectively, where the zero-point offset between the Hα and Hβ masses ($\Delta_{\rm zpt}$), intrinsic scatter with respect to a one-to-one relation ($\sigma_{\rm int}$), and the fraction of the data points where 1σ errors of $M_{\rm BH}$ values from different estimators overlap with each other ($p_{\rm con}$) are shown. We find that the masses from our estimators are closer to a one-to-one relation than of G05 or S11, throughout the range $10^{6-10}\, M_\odot$. Also, fully considering the propagated errors in the mass equation, our estimators may overestimate the $M_{\rm BH}$ uncertainty when comparing the Hβ and Hα masses as reflected from the negative $\sigma_{\rm int}$, which suggests that the actual difference in the *f* factor or $R_{\rm BLR}$ between the Hβ and Hα line emitting regions are likely to be smaller than their uncertainty. Therefore, we regard the Hβ and Hα $M_{\rm BH}$ from our estimators to be indistinguishable, which is supported by the high fraction (98%) of Hβ/Hα masses to be consistent within measurement error.

With the Hβ and Hα $M_{\rm BH}$ recipes checked to be mutually consistent, we further compare the Balmer to the UV-based $M_{\rm BH}$ with $\Delta M_{\rm BH} < 0.3$ dex in Figure 15. We use $M_{\rm BH,H\alpha}$ as the Balmer mass because of the stronger Hα emission than Hβ and the availability of the Hα line in our *AKARI* data, unless only

the $M_{\rm BH,H\beta}$ can be estimated using the measurements in the literature. Compared to the conventional estimators calibrated at relatively low luminosity and redshift (McLure & Dunlop 2004; Vestergaard & Peterson 2006) or relatively high luminosity and redshift (S12), our calibrations (Equations (6), (7), (9), and (10)) bring the rest-UV (Mg II in Figures 15(a)–(c), C IV in Figures 15(d)–(f)) and Balmer $M_{\rm BH}$s to be closer to a one-to-one relation in the range $10^{7-10}\,M_\odot$ in terms of both zero-point offset and intrinsic scatter. Also, we find that our $M_{\rm BH}$ estimators, fully considering the propagated errors, give a more realistic value of the error bars compared to estimators that do not and raise the $p_{\rm con}$. Moreover, previous UV-based $M_{\rm BH}$s are tilted to ours largely from the different slope of the FWHM term from that of our estimator (e.g., 0.24 in S12, 2.11 in this work for C IV; see also Park et al. 2013), and this produces a systematic offset in the $M_{\rm BH}$ values. For example, we find that S12 estimators produce a systematic difference between C IV and Balmer $M_{\rm BH}$ in such a way that $M_{\rm BH,C_{IV}}$ are larger by 0.7 dex at $M_{\rm BH,H\alpha/H\beta} = 10^7\,M_\odot$ and smaller by 0.4 dex at $M_{\rm BH,H\alpha/H\beta} = 10^{10}\,M_\odot$ (Figure 15(e)). Previous UV-based $M_{\rm BH}$ calibrations from a limited dynamic range yields $\sigma_{\rm int}$ to the Balmer $M_{\rm BH}$ as small as our estimator and may place the C IV and Balmer masses to be consistent within a narrow range of masses, but we caution on the usage of conventional estimators when extensively comparing the rest-optical and UV $M_{\rm BH}$.

Even when using our rest-UV mass equations with a minimized zero point and systematic offsets from a large dynamic range, the intrinsic scatter is another issue. Although our $\sigma_{\rm int}$ of the $M_{\rm BH,Mg_{II}}$ to the Balmer $M_{\rm BH}$ is relatively small (0.09 dex), the $\sigma_{\rm int}$ of the $M_{\rm BH,C_{IV}}$ to the Balmer $M_{\rm BH}$ (0.40 dex) is comparable to the systematic uncertainty of the single-epoch mass estimator itself (Bentz et al. 2013; Woo et al. 2013). Moreover, because our estimators take into account the measurement error of the f factor, R–L relation, scatter in the UV–optical luminosity, and line width relations, the nonnegligible fraction of rest-UV masses that deviate from the Balmer masses more than their overlapping measurement errors (13% of the $M_{\rm BH,Mg_{II}}$ and 41% of the $M_{\rm BH,C_{IV}}$) suggests that one needs to be cautious about the usage of the C IV line when deriving $M_{\rm BH}$ values.

5. DISCUSSION

5.1. Reliability of Single-epoch AGN BH Masses

Do the relations between continuum and line luminosities, and the FWHM relations that hold up to the highest luminosity AGNs, guarantee the accurate mass estimation of the most luminous AGNs? Unfortunately, the answer is not clear yet because the $R_{\rm BLR,H\beta}$–L_{5100} relation is not observationally probed for $L_{5100} > 10^{46}$ ergs s^{-1} (Bentz et al. 2013). A hint to estimate the behavior of the high-luminosity end of the optical R–L relation is to look at the $R_{\rm BLR,C_{IV}}$–L_{1350} relation, where the $R_{\rm BLR,C_{IV}}$ traces the inner part to the Hβ line region. Although the current number of C IV reverberation measurements is small (Kaspi et al. 2007; Sluse et al. 2011; Chelouche et al. 2012), they cover up to luminosities of $L_{1350} = 10^{47.0}$ ergs s^{-1} and $L_{5100} = 10^{46.8}$ ergs s^{-1}. The slope of the relation in Kaspi et al. (2007), $(0.52–0.55) \pm 0.04$, is within the uncertainty to the slope of the $R_{\rm BLR,H\beta}$–L_{5100} relation (Bentz et al. 2013), 0.533 ± 0.034. This suggests that the ratio of $R_{\rm BLR,H\beta}$ to $R_{\rm BLR,C_{IV}}$ is nearly a constant at two to four over $L_{5100} < 10^{46}$ ergs s^{-1}, where the proportionality of L_{5100} and L_{1350} suggests that it is likely so at a higher luminosity range. Therefore, we do not expect a break in the luminous-end optical R–L relation unless the optical data will somehow fail to form a simple relation at high luminosity where the current UV relation holds. Future compilations of both the C IV and Hβ BLR sizes will help to better constrain the luminous-end R–L relation.

Even if we find it plausible to assume that the $R_{\rm BLR,H\beta}$–L_{5100} relation does not change its slope in the luminous end, the large scatter in between the Balmer and rest-UV $M_{\rm BH}$ imposes further limitations on the usage of UV $M_{\rm BH}$ estimators. As discussed in the introduction, it has been known that there is a large $\sigma_{\rm int}$ in the C IV and Balmer $M_{\rm BH}$ relation in comparison to that of the Mg II and Balmer. Our comparison of $M_{\rm BH,H\alpha}$ against $M_{\rm BH,C_{IV}}$ for high-luminosity AGNs at $z > 3.3$ further shows consistent results. Indeed, we find four out of 11 $M_{\rm BH,C_{IV}}$ of *AKARI* quasars in Figure 15(f) to be scattered to the $M_{\rm BH,H\alpha}$ by an order of magnitude or larger, so the use of C IV masses can be questioned up to the highest redshifts even when considering the additional uncertainties in the *AKARI* $M_{\rm BH,H\alpha}$ tested in Figure 5. Overall, our result supports that the $M_{\rm BH}$ estimate from C IV contains a rather large uncertainty at any redshift or luminosity.

The greatest uncertainties when calibrating the UV $M_{\rm BH}$ estimators in this work ($\sigma_{\rm int} > 0.1$ dex) come from the scatter in the L_{5100}–L_{1350} and FWHM$_{\rm H\beta}$–FWHM$_{\rm C_{IV}}$ relations. Because a variety of obscurations in the rest-UV continuum of quasars may result in a scattered L_{5100}–L_{1350} relation, we suggest taking into account the level of obscuration when establishing the $M_{\rm BH,C_{IV}}$ estimator, although careful treatment is required because it is controversial whether the color correction into the $M_{\rm BH}$ works to reduce the scatter between the C IV and Balmer masses (Assef et al. 2011; S12). Meanwhile, the scatter in the FWHM relations, which is the largest for the FWHM$_{\rm H\beta}$–FWHM$_{\rm C_{IV}}$ relation, could arise from broad absorption features or a nonreverberating component of the C IV broad emission (Denney 2012), where future reverberation mapping will further enable us to test. Without a detailed analysis on the origin of the scatter in between the Balmer and rest-UV $M_{\rm BH}$, we caution on the individual measurement of $M_{\rm BH}$ from UV, especially the one using C IV.

5.2. On the Massive End BH Mass Evolution

Having cross-calibrated the $M_{\rm BH}$ estimators, we plot the Balmer and Mg II $M_{\rm BH}$ measurements of quasars along redshift in Figure 16(a) from our *AKARI* observations and the literature indicated on the figure. First of all, we notice that the most massive envelope, which stays at $\sim 10^{10}\,M_\odot$ up to $z\sim5$, starts to disappear at higher redshift. To quantify how significant the $M_{\rm BH}$s are evolving at the massive end for $z > 5$ quasars, we performed the Kolmogorov–Smirnov (K–S) test to compare the mass distribution at above and below $z = 5$ at $M_{\rm BH} > 2 \times 10^9\,M_\odot$. This mass threshold for completeness is governed by the shallow *AKARI* data, through the $L_{5100} \gtrsim 10^{46.5}$ ergs s^{-1} limit at S/N$_{\rm H\alpha}$ = 3 and the FWHM limit of 2500 km s^{-1} from Section 3.1. The K–S probability $p_{\rm KS} = 0.34\%$ turns out to be meaningfully small, supporting the massive end BHs at $z < 5$ to be heavier than at $z > 5$. We checked our results to be unchanged much by the inclusion of

AKARI data that could bias the masses by up to ∼0.1 dex (Section 3.1), by performing the same test while giving a −0.1 dex correction to the *AKARI* data, only to find the trend to be mildly weaker ($p_{KS} = 0.64\%$).

We cross-check if this evolution in M_{BH} is also reflected through the M_{BH} histograms. In order to correct for the luminosity selection effect in number counting, we plot the 1450 Å absolute magnitude (M_{1450}) histogram in Figure 16(b). We overplot the quasar luminosity functions in redshift bins of $2 < z < 3$, $3 < z < 5$, and $z > 5$, scaled by a constant so that they match the M_{1450} counts in total number at $M_{1450} < -26.4$. We use only the $M_{1450} < -26.4$ data for better completeness in scaling the luminosities. The break luminosity (M_{1450}), the faint end slope (α), and the bright end slope (β) of the luminosity function are fixed to $M_{1450} = -26.39$ at $z > 3$ and $M_{1450} = -25.5$ at $z < 3$ while $(\alpha, \beta) = (-1.80, -3.26)$ at all redshifts (McGreer et al. 2013; Ross et al. 2013). The set of (α, β) is fixed because the evolution in the α value does not affect the luminosity regime of interest much, and β stays nearly constant with redshift. Overall, we find that the quasar samples at $z < 5$ are in excess of luminous objects compared to the luminosity functions.

Not only there is a luminosity selection effect in the quasars plotted in Figure 16(a), there is also a FWHM limit for each reference data point that is the poorest for the *AKARI* data. Taking into account these effects, we plot the M_{BH} histograms in Figure 16(c) before (points) and after (histograms) applying the luminosity selection correction and a FWHM = 2500 km s^{-1} cut. After correcting the luminosity selection and giving the FWHM cut, the M_{BH} distribution is shifted to more $10^9\,M_\odot$ BHs and less $10^{10}\,M_\odot$ BHs at $z < 5$. Still, the number of $10^{10}\,M_\odot$ BHs start to drop at $z > 5$, whereas the $10^9\,M_\odot$ BHs do not exhibit an evolution up to the Poisson error. Thus, we interpret the M_{BH} histogram as showing that there is an evolution in the number of $10^{10}\,M_\odot$ BHs increasing with time at $z > 5$. The $z > 5$, $\sim 10^9\,M_\odot$ AGNs are likely to be in a rapidly growing state such that their masses can soon reach $\sim 10^{10}\,M_\odot$, consistent with the higher Eddington ratio trend found in distant, luminous AGNs (Willott et al. 2010a; De Rosa et al. 2011). Note that the number density of quasars evolves strongly in $z = 2$–6 (e.g., Willott et al. 2010a). We caution that the mass and luminosity histograms in Figures 16(b) and (c) do not reflect this number density evolution and that Figures 16(b) and (c) are used for comparing the shape of these functions. The numbers of $z = 2$–6 quasars appear similar in these figures because the sampling of quasars is different at each redshift bin.

We further investigate the upper mass envelope of $z > 5$ AGNs to check if their extremely high masses can be explained by the earliest BH growth from model seed masses. For this we follow Volonteri & Rees (2005) to assume a continuous, Eddington-limited accretion of matter to a BH seed at $z = 20$, where the BH will grow with time as Equation (1), with $t_0 = t_{z=20}$ and $M_0 = M_{z=20}$ for the age of the universe and the seed BH mass, respectively, at $z = 20$. For each given $\epsilon = 0.05$, 0.1, 0.2, we determined a pair of seed masses M_0 such that the growth curve reaches the observed massive limit at $z \sim 5$ and $z \sim 7$ respectively, shown in Figure 16(a).

When $\epsilon = 0.05$, the seed masses to explain the most massive BHs at $z \sim 5$ and 7 are $M_0 \sim 10^{-12}\,M_\odot$ and $10^{-4}\,M_\odot$, respectively, which, in other words, gives plenty of time for seed BHs of any meaningful mass to grow up to the most massive quasars without a strictly continuous, Eddington-limited accretion. One can expect to find fully grown massive BHs at $z \sim 6$ detectable as high or low Eddington ratio AGNs, if such rapid growth is possible. Luminous AGNs at $z \sim 6$ have high Eddington ratios so far, but future studies may uncover fainter objects with weakly active BHs. If $\epsilon = 0.1$, which is roughly consistent with the Soltan argument measurements (Soltan 1982; Yu & Tremaine 2002), it predicts $M_0 \sim 10^{1-3}\,M_\odot$, which gives a reasonable estimate of the seed mass to be Population III stars. However, it may be difficult for stellar seed BHs to keep their Eddington-limited accretion from $z = 20$ to 7–5, which is 0.6–1.0 Gyrs in duration and is longer than a typical quasar lifetime ($\lesssim$0.1 Gyr, Hopkins et al. 2005), perhaps requiring an extended period of accretion or BH–BH mergers. Lastly, the $\epsilon = 0.2$ model that corresponds to the case when BHs are rotating rapidly (e.g., Kerr 1963; Marconi et al. 2004) only accepts very heavy seed BHs at $M_0 \sim 10^{5.7-6.6}\,M_\odot$, requiring supercritical accretion from lighter seed masses (Volonteri & Rees 2005) or supporting - direct collapse of massive primordial gas (Volonteri et al. 2008). With $\epsilon = 0.2$, we expect that the most massive $\sim 10^{10}\,M_\odot$ BHs from $M_0 \sim 10^6\,M_\odot$ seeds can only start appearing at the redshifts between 5 and 6.

6. SUMMARY

We measured the redshifted Hα emission and rest-UV to rest-optical continuum properties of 155 luminous quasars at $3 \lesssim z \lesssim 6$ using the *AKARI* spectra and other data sets and estimated their M_{BH}. We summarize our findings as follows.

1. The L_{5100}–$L_{H\alpha}$ relation holds up to the most luminous quasars ($L_{5100} \sim 10^{47}$ ergs s^{-1}) with a single slope unchanging up to $z \sim 6$, suggesting a consistent response of the BLR to the incident continuum, irrespective of AGN luminosity and redshift.
2. The relations between rest-optical and UV continuum and line luminosities and the FWHM relations hold up to the highest luminosity AGNs. Together with predictions of an extended optical *R–L* relation to the highest luminosities, it enables us to calibrate the rest-UV M_{BH} estimators to be consistent with the Balmer masses overall. However, some of the rest-UV and optical M_{BH} are scattered more than their uncertainties, including the errors from the recipe, for only 13% of Mg II masses but for 41% of the C IV estimation. The C IV masses have a 0.40 dex intrinsic scatter to the Balmer masses, which places negative implications on its reliability.
3. The massive end envelope of M_{BH} steeply evolves at $z > 5$, suggesting they are in a rapidly growing state from given seed masses. The most massive BHs at $z = 5$–7 can be explained by the Eddington-limited, continuous accretion onto $\sim 10^{1-3}\,M_\odot$ seed masses at $z = 20$ if $\epsilon = 0.1$ and the formation redshift is $z = 20$ for the seed BH, whereas there are a range of viable accretion rates and seed masses if ϵ is different.

We expect future observations to compile sensitive measurements of (L_{5100}, $L_{H\alpha}$) to better identify the outliers in the L_{5100}–$L_{H\alpha}$ relation, where an example would be a small population of weak emission line quasars. Also, future rest-optical reverberation mapping of high luminosity AGNs will verify if the prediction for the *R–L* relation to extend with a single

slope will hold. Most importantly, the discovery of the highest redshift quasars will further uncover the evolutionary tracks of the earliest BH growth, also improving the current understanding of $M_{\rm BH}$ growth at $z > 5$ from small-number statistics.

We thank Todd Boroson, Jenny Greene, Lisa Storrie-Lombardi, Celine Péroux, and Donald Schneider for kindly providing the iron template derived from I Zw 1, the rest-frame optical luminosities and line widths of local AGNs, and the optical spectra of APM-UKST quasars and Q0000–26. Also, we thank Eduardo Bañados, Hyunjin Shim, and Doosoo Yoon for useful communication. This research was supported by an appointment to the NASA Postdoctoral Program at the Jet Propulsion Laboratory, administered by Oak Ridge Associated Universities through a contract with NASA. This work was supported by the National Research Foundation of Korea (NRF) grant No. 2008-0060544 (H. D. J. and M. I.), 2012R1A2A2A01006087 (J. H. W), 2012R1A4A1028713 (H. M. L. and M. G. L.), and NRF-2014-Fostering Core Leaders of Future Program, No. 2014-009728 (D.K.), funded by the Korea government (MSIP). This work was supported by grant *MOST*100-2112-M-001-001-MY3 (Y. O.).

This research is based on observations with *AKARI*, a JAXA project with the participation of ESA. Funding for SDSS-III has been provided by the Alfred P. Sloan Foundation, the participating institutions, the National Science Foundation, and the U.S. Department of Energy Office of Science. The SDSS-III web site is http://www.sdss3.org/. SDSS-III is managed by the Astrophysical Research Consortium for the participating institutions of the SDSS-III Collaboration, including the University of Arizona, the Brazilian Participation Group, Brookhaven National Laboratory, Carnegie Mellon University, University of Florida, the French Participation Group, the German Participation Group, Harvard University, the Instituto de Astrofisica de Canarias, the Michigan State/Notre Dame/JINA Participation Group, Johns Hopkins University, Lawrence Berkeley National Laboratory, Max Planck Institute for Astrophysics, Max Planck Institute for Extraterrestrial Physics, New Mexico State University, New York University, Ohio State University, Pennsylvania State University, University of Portsmouth, Princeton University, the Spanish Participation Group, University of Tokyo, University of Utah, Vanderbilt University, University of Virginia, University of Washington, and Yale University. This publication makes use of data products from the Two Micron All Sky Survey, which is a joint project of the University of Massachusetts and the Infrared Processing and Analysis Center/California Institute of Technology, funded by the National Aeronautics and Space Administration and the National Science Foundation. This publication makes use of data products from the United Kingdom Infrared Deep Sky Survey. The UKIDSS project is defined in Lawrence et al. (2007). UKIDSS uses the UKIRT Wide Field Camera (WFCAM; Casali et al. 2007). The photometric system is described in Hewett et al. (2006), and the calibration is described in Hodgkin et al. (2009). The pipeline processing and science archive are described in M. J. Irwin et al. (2009, in preparation) and Hambly et al. (2008). This publication makes use of data products from the Wide-field Infrared Survey Explorer, which is a joint project of the University of California, Los Angeles, and the Jet Propulsion Laboratory/California Institute of Technology, funded by the National Aeronautics and Space Administration.

REFERENCES

Ahn, C. P., Alexandroff, R., Allende Prieto, C., et al. 2012, ApJS, 203, 21
Ahn, C. P., Alexandroff, R., Allende Prieto, C., et al. 2014, ApJS, 211, 17
Akritas, M. G., & Bershady, M. A. 1996, ApJ, 470, 706
Assef, R. J., Denney, K. D., Kochanek, C. S., et al. 2011, ApJ, 742, 93
Bañados, E., Venemans, B. P., Morganson, E., et al. 2014, AJ, 148, 14
Baskin, A., & Laor, A. 2005, MNRAS, 356, 1029
Begelman, M. C., Volonteri, M., & Rees, M. J. 2006, MNRAS, 370, 289
Bellovary, J., Volonteri, M., Governato, F., et al. 2011, ApJL, 742, L13
Bentz, M. C., Denney, K. D., Grier, C. J., et al. 2013, ApJ, 767, 149
Bonifacio, P., Monai, S., & Beers, T. C. 2000, AJ, 120, 2065
Boroson, T. A., & Green, R. F. 1992, ApJS, 80, 109
Boyle, B. J., Shanks, T., Croom, S. M., et al. 2000, MNRAS, 317, 1014
Bromm, V., & Loeb, A. 2003, ApJL, 596, L34
Casali, M., Adamson, A., Alves de Oliveira, C., et al. 2007, A&A, 467, 777
Chelouche, D., Daniel, E., & Kaspi, S. 2012, ApJL, 750, L43
Collin, S., Kawaguchi, T., Peterson, B. M., & Vestergaard, M. 2006, A&A, 456, 75
Cool, R. J., Kochanek, C. S., Eisenstein, D. J., et al. 2006, AJ, 132, 823
Denney, K. D., Peterson, B. M., Dietrich, M., Vestergaard, M., & Bentz, M. C. 2009, ApJ, 692, 246
Denney, K. D. 2012, ApJ, 759, 44
De Rosa, G., Decarli, R., Walter, F., et al. 2011, ApJ, 739, 56
De Rosa, G., Venemans, B. P., Decarli, R., et al. 2014, ApJ, 790, 145
Diamond-Stanic, A. M., Fan, X., Brandt, W. N., et al. 2009, ApJ, 699, 782
Dietrich, M., Mathur, S., Grupe, D., & Komossa, S. 2009, ApJ, 696, 1998
Djorgovski, S. G., Gal, R. R., Odewahn, S. C., et al. 1998, in Wide Field Surveys in Cosmology, ed. S. Colombi, Y. Mellier, & B. Raban (Paris: Editions Frontieres), 89
Dunlop, J. S., & Peacock, J. A. 1990, MNRAS, 247, 19
Fan, X., Hennawi, J. F., Richards, G. T., et al. 2004, AJ, 128, 515
Fan, X., Narayanan, V. K., Lupton, R. H., et al. 2001, AJ, 122, 2833
Fan, X., Strauss, M. A., Gunn, J. E., et al. 1999, ApJL, 526, L57
Fan, X., Strauss, M. A., Richards, G. T., et al. 2006, AJ, 131, 1203
Fan, X., Strauss, M. A., Schneider, D. P., et al. 2003, AJ, 125, 1649
Fan, X., White, R. L., Davis, M., et al. 2000, AJ, 120, 1167
Glikman, E., Helfand, D. J., & White, R. L. 2006, ApJ, 640, 579
Goto, T. 2006, MNRAS, 371, 769
Greene, J. E., & Ho, L. C. 2005, ApJ, 630, 122
Gregory, P. C., & Condon, J. J. 1991, ApJS, 75, 1011
Griffith, M. R., Wright, A. E., Burke, B. F., & Ekers, R. D. 1995, ApJS, 97, 347
Hambly, N. C., Collins, R. S., Cross, N. J. G., et al. 2008, MNRAS, 384, 637
Henry, J. P., Gioia, I. M., Boehringer, H., et al. 1994, AJ, 107, 1270
Hewett, P. C., Foltz, C. B., & Chaffee, F. H. 1995, AJ, 109, 1498
Hewett, P. C., Warren, S. J., Leggett, S. K., & Hodgkin, S. T. 2006, MNRAS, 367, 454
Hines, D. C., Krause, O., Rieke, G. H., et al. 2006, ApJL, 641, L85
Ho, L. C., Goldoni, P., Dong, X.-B., Greene, J. E., & Ponti, G. 2012, ApJ, 754, 11
Hodgkin, S. T., Irwin, M. J., Hewett, P. C., & Warren, S. J. 2009, MNRAS, 394, 675
Hopkins, P. F., Hernquist, L., Martini, P., et al. 2005, ApJL, 625, L71
Im, M., Lee, I., Cho, Y., et al. 2007, ApJ, 664, 64
Im, M. 2010, in IAU Symp. 267, Co-Evolution of Central Black Holes and Galaxies, ed. B. M. Peterson, R. S. Somerville, & T. Storchi-Bersmann (Cambridge: Cambridge Univ. Press), 40
Jiang, L., Fan, X., Brandt, W. N., et al. 2010, Natur, 464, 380
Jiang, L., Fan, X., Hines, D. C., et al. 2006, AJ, 132, 2127
Jiang, L., Fan, X., Vestergaard, M., et al. 2007, AJ, 134, 1150
Jun, H. D., & Im, M. 2013, ApJ, 779, 104
Jun, H. D., Im, M., & Lee, H. M., AKARI QSONG Team 2012, PKAS, 27, 361
Kaspi, S., Brandt, W. N., Maoz, D., et al. 2007, ApJ, 659, 997
Kaspi, S., Maoz, D., Netzer, H., et al. 2005, ApJ, 629, 61
Kaspi, S., Smith, P. S., Netzer, H., et al. 2000, ApJ, 533, 631
Kennefick, J. D., Djorgovski, S. G., & de Carvalho, R. R. 1995, AJ, 110, 2553
Kerr, R. P. 1963, PhRvL, 11, 237
Kim, D., Im, M., Kim, J. H., et al. 2015, ApJS, 216, 17
Kurk, J. D., Walter, F., Fan, X., et al. 2007, ApJ, 669, 32
Laor, A., Bahcall, J. N., Jannuzi, B. T., et al. 1994, ApJ, 420, 110
Laor, A., & Davis, S. W. 2011, MNRAS, 417, 681
Lawrence, A., Warren, S. J., Almaini, O., et al. 2007, MNRAS, 379, 1599
Lee, I., Im, M., Kim, M., et al. 2008, ApJS, 175, 116
Leipski, C., Meisenheimer, K., Walter, F., et al. 2014, ApJ, 785, 154

Lodato, G., & Natarajan, P. 2006, MNRAS, 371, 1813
Madau, P., Haardt, F., & Dotti, M. 2014, ApJL, 784, L38
Marconi, A., Risaliti, G., Gilli, R., et al. 2004, MNRAS, 351, 169
Matsuoka, K., Silverman, J. D., Schramm, M., et al. 2013, ApJ, 771, 64
McGill, K. L., Woo, J.-H., Treu, T., & Malkan, M. A. 2008, ApJ, 673, 703
McGreer, I. D., Becker, R. H., Helfand, D. J., & White, R. L. 2006, ApJ, 652, 157
McGreer, I. D., Jiang, L., Fan, X., et al. 2013, ApJ, 768, 105
McLure, R. J., & Dunlop, J. S. 2004, MNRAS, 352, 1390
McLure, R. J., & Jarvis, M. J. 2002, MNRAS, 337, 109
Mortlock, D. J., Warren, S. J., Venemans, B. P., et al. 2011, Natur, 474, 616
Murakami, H., Baba, H., Barthel, P., et al. 2007, PASJ, 59, 369
Natarajan, P. 2014, GReGr, 46, 1702
Netzer, H., Lira, P., Trakhtenbrot, B., Shemmer, O., & Cury, I. 2007, ApJ, 671, 1256
Ohyama, Y., Onaka, T., Matsuhara, H., et al. 2007, PASJ, 59, 411
Onaka, T., Matsuhara, H., Wada, T., et al. 2007, PASJ, 59, 401
Osterbrock, D. E 1989, Astrophysics of Gaseous Nebulae and Active Galactic Nuclei (Mill Valley, CA: Univ. Science Books)
Oyabu, S., Kawara, K., Tsuzuki, Y., et al. 2009, ApJ, 697, 452
Oyabu, S., Wada, T., Ohyama, Y., et al. 2007, PASJ, 59, 497
Park, D., Woo, J.-H., Denney, K. D., & Shin, J. 2013, ApJ, 770, 87
Péroux, C., Storrie-Lombardi, L. J., McMahon, R. G., Irwin, M., & Hook, I. M. 2001, AJ, 121, 1799
Peterson, B. M., Ferrarese, L., Gilbert, K. M., et al. 2004, ApJ, 613, 682
Planck Collaboration, Ade, P. A. R., Aghanim, N., et al. 2014, A&A, 571, AA16
Rengstorf, A. W., Mufson, S. L., Abad, C., et al. 2004, ApJ, 606, 741
Richards, G. T., Fan, X., Newberg, H. J., et al. 2002, AJ, 123, 2945
Richards, G. T., Strauss, M. A., Fan, X., et al. 2006, AJ, 131, 2766
Ross, N. P., McGreer, I. D., White, M., et al. 2013, ApJ, 773, 14
Sakon, I., Onaka, T., Ootsubo, T., Matsuhara, H., & Noble, J. 2012, Proc. SPIE, 8442, 844244
Schlegel, D. J., Finkbeiner, D. P., & Davis, M. 1998, ApJ, 500, 525
Schmidt, M., & Green, R. F. 1983, ApJ, 269, 352
Schmidt, M., Schneider, D. P., & Gunn, J. E. 1995, AJ, 110, 68
Schneider, D. P., Hall, P. B., Richards, G. T., et al. 2007, AJ, 134, 102
Schneider, D. P., Richards, G. T., Hall, P. B., et al. 2010, AJ, 139, 2360
Schneider, D. P., Schmidt, M., & Gunn, J. E. 1989, AJ, 98, 1507
Sedgwick, C., Serjeant, S., Pearson, C., et al. 2013, MNRAS, 436, 395
Shang, Z., Wills, B. J., Wills, D., & Brotherton, M. S. 2007, AJ, 134, 294
Shemmer, O., Netzer, H., Maiolino, R., et al. 2004, ApJ, 614, 547
Shen, Y., Greene, J. E., Strauss, M. A., Richards, G. T., & Schneider, D. P. 2008, ApJ, 680, 169
Shen, Y., & Liu, X. 2012, ApJ, 753, 125
Shen, Y., Richards, G. T., Strauss, M. A., et al. 2011, ApJS, 194, 45
Skrutskie, M. F., Cutri, R. M., Stiening, R., et al. 2006, AJ, 131, 1163
Sluse, D., Schmidt, R., Courbin, F., et al. 2011, A&A, 528, A100
Soltan, A. 1982, MNRAS, 200, 115
Stern, D., Kirkpatrick, J. D., Allen, L. E., et al. 2007, ApJ, 663, 677
Storrie-Lombardi, L. J., Irwin, M. J., McMahon, R. G., & Hook, I. M. 2001, MNRAS, 322, 933
Storrie-Lombardi, L. J., McMahon, R. G., Irwin, M. J., & Hazard, C. 1996, ApJ, 468, 121
Sulentic, J. W., Bachev, R., Marziani, P., Negrete, C. A., & Dultzin, D. 2007, ApJ, 666, 757
Trakhtenbrot, B., Netzer, H., Lira, P., & Shemmer, O. 2011, ApJ, 730, 7
Tremaine, S., Gebhardt, K., Bender, R., et al. 2002, ApJ, 574, 740
van Dokkum, P. G. 2001, PASP, 113, 1420
Vanden Berk, D. E., Richards, G. T., Bauer, A., et al. 2001, AJ, 122, 549
Venemans, B. P., Findlay, J. R., Sutherland, W. J., et al. 2013, ApJ, 779, 24
Vestergaard, M. 2004, ApJ, 601, 676
Vestergaard, M., Fan, X., Tremonti, C. A., Osmer, P. S., & Richards, G. T. 2008, ApJL, 674, L1
Vestergaard, M., & Osmer, P. S. 2009, ApJ, 699, 800
Vestergaard, M., & Peterson, B. M. 2006, ApJ, 641, 689
Volonteri, M., Lodato, G., & Natarajan, P. 2008, MNRAS, 383, 1079
Volonteri, M., & Rees, M. J. 2005, ApJ, 633, 624
Wang, J.-G., Dong, X.-B., Wang, T.-G., et al. 2009, ApJ, 707, 1334
Wang, J.-M., Du, P., Li, Y.-R., et al. 2014, ApJL, 792, L13
Warren, S. J., Hewett, P. C., & Osmer, P. S. 1994, ApJ, 421, 412
Webb, J. K., Parnell, H. C., Carswell, R. F., McMahon, R. G., & Irwin, M. J. 1988, Msngr, 51, 15
Willott, C. J., Albert, L., Arzoumanian, D., et al. 2010a, AJ, 140, 546
Willott, C. J., Delorme, P., Omont, A., et al. 2007, AJ, 134, 2435
Willott, C. J., Delorme, P., Reylé, C., et al. 2010b, AJ, 139, 906
Woo, J.-H., Schulze, A., Park, D., et al. 2013, ApJ, 772, 49
Wright, E. L., Eisenhardt, P. R. M., Mainzer, A. K., et al. 2010, AJ, 140, 1868
Wu, X.-B., Jia, Z.-D., Chen, Z.-Y., et al. 2010, RAA, 10, 745
Wu, X.-B., Wang, F., Fan, X., et al. 2015, Natur, 518, 512
Wyithe, J. S. B., & Loeb, A. 2012, MNRAS, 425, 2892
York, D. G., Adelman, J., Anderson, J. E., Jr., et al. 2000, AJ, 120, 1579
Yu, Q., & Tremaine, S. 2002, MNRAS, 335, 965